iScience

CellPress

Article

Interfacial Contact Passivation for Efficient and Stable Cesium-Formamidinium Double-Cation Lead Halide Perovskite Solar Cells

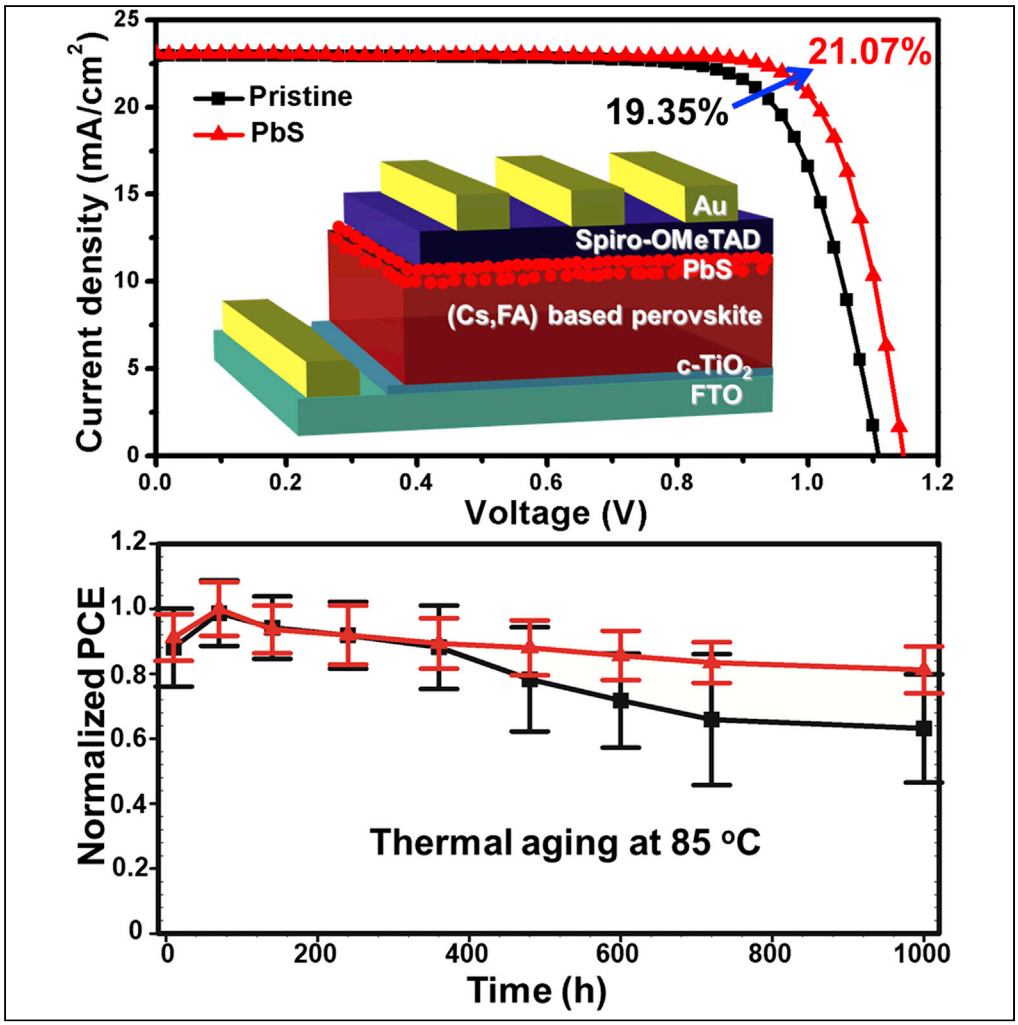

Yu Chen, Jianchao Yang, Shubo Wang, Yihui Wu, Ningyi Yuan, Wen-Hua Zhang

yihuiwu@caep.cn (Y.W.)
nyyuan@cczu.edu.cn (N.Y.)
whzhang@caep.cn (W.-H.Z.)

HIGHLIGHTS

An *in situ* interfacial defects contact passivation strategy has been developed

PbS quantum dots were used as the passivant to reduce the traps of perovskite films

The methylammonium-free device with passivation layer gives efficiency over 21%

The unsealed device demonstrated excellent ambient and thermal long-term stability

Chen et al., iScience *23*, 100762
January 24, 2020
https://doi.org/10.1016/j.isci.2019.100762

iScience

CellPress

Article

Interfacial Contact Passivation for Efficient and Stable Cesium-Formamidinium Double-Cation Lead Halide Perovskite Solar Cells

Yu Chen,[1,2,3] Jianchao Yang,[1,2,3] Shubo Wang,[1] Yihui Wu,[1,2,*] Ningyi Yuan,[1,4,*] and Wen-Hua Zhang[2,*]

SUMMARY

Perovskite solar cells (PSCs) have achieved extremely high power conversion efficiencies (PCEs) of over 25%, but practical application still requires further improvement in the long-term stability of the device. Herein, we present an *in situ* interfacial contact passivation strategy to reduce the interfacial defects and extraction losses between the hole transporting layer and perovskite. The existence of PbS promotes the crystallization of perovskite, passivates the interface and grain boundary defects, and reduces the nonradiation recombination, thereby leading to a champion PCE of 21.07% with reduced hysteresis, which is one of the best results for the methylammonium (MA)-free, cesium formamidinium double-cation lead-based PSCs. Moreover, the unencapsulated device retains more than 93% and 82% of its original efficiencies after 1 year's storage under ambient conditions and thermal aging at 85°C for 1,000 h in a nitrogen atmosphere, likely due to the usage of MA-free perovskite and the enhanced surface hydrophobicity.

INTRODUCTION

Perovskite solar cells (PSCs) have drawn intense research interest due to their excellent optoelectronic properties and ease of fabrication (Kojima et al., 2009; Zhang et al., 2016; Brenner et al., 2016; Yang et al., 2018). Tremendous efforts from different groups have boosted the power conversion efficiencies (PCEs) of PSCs from 3.8% to over 25% in just a few years, making perovskite one of the most promising photovoltaic (PV) materials (NREL Chart.). However, long-term stability is still limiting the practical application of PSCs, which is partly related to the usage of methylammonium (MA)-containing perovskite (Wang et al., 2019). The instability of $MAPbI_3$ is ascribed to the degradation of CH_3NH_3I into CH_3I and NH_3 at temperature as low as 80°C (Turren-Cruz et al., 2018). Fortunately, the pure formamidinium (FA)-based perovskite exhibits higher thermal stability and narrower band gaps (1.48 eV) than the MA-containing perovskite (Lee et al., 2015), showing great application potentials in PV area. Nevertheless, the pure FA-based perovskite is traditionally prone to form photo-inactive phase (yellow phase) at room temperature; the photoactive phase (black phase) can only be obtained at high temperature (more than 150°C). Although many works have been performed on avoiding the yellow phase of FA-based perovskite by doping with small amount of Cs^+ and/or Rb^+, the PCEs of the MA-free PSCs are still not satisfactory compared with the PCEs of MA-containing PSCs (Turren-Cruz et al., 2018; Wu et al., 2018; Chen et al., 2018, 2019a). Much effort should thus be devoted to elevate the performance of MA-free, FA-based PSCs.

In addition, the device stability is also reported to be related to the imperfect contact and carrier recombination at the interfaces and grain boundaries (GBs). Owing to the low formation energy and poor thermal stability, presence of a large number of defects at the interfaces and GBs within the polycrystalline perovskite is unavoidable (Zheng et al., 2017; Niu et al., 2018). In fact, defects can enhance non-radiative recombination, seriously reducing charge-carrier lifetime and photoluminescence (PL) yield. In addition, these defects form convenient channels for moisture or oxygen diffusion and ion migration, lead to the grain degradation, and decrease the stability of PSCs (Liu et al., 2018; Zheng et al., 2018). Therefore, it is highly crucial to passivate the defects at the surface and the GB to further boost the PCE, and to prolong the durability of PSCs. Interfacial engineering of perovskite film by inserting an interfacial layer, such as methimazole (Liu et al., 2018), quaternary ammonium halide (Zheng et al., 2017), π-conjugated Lewis base (Lin et al., 2017; Qin et al., 2018), organic semiconductor polymer (Wu et al., 2016, 2018), organic halide salt (Jiang et al., 2019), wide band-gap perovskite (Cho et al., 2017), or two-dimensional perovskite materials (Cho et al., 2018), between the perovskite and the charge transport layers has been the widely used method to eliminate the interfacial trap states and improve the device stability. These modifications of the

[1]Jiangsu Province Cultivation Base for State Key Laboratory of Photovoltaic Science and Technology, Changzhou University, Changzhou, Jiangsu 213164, China

[2]Sichuan Research Center of New Materials, Institute of Chemical Materials, China Academy of Engineering Physics, 596 Yinhe Road, Shuangliu, Chengdu 610200, China

[3]These authors contributed equally

[4]Lead Contact

*Correspondence: yihuiwu@caep.cn (Y.W.), nyyuan@cczu.edu.cn (N.Y.), whzhang@caep.cn (W.-H.Z.)

https://doi.org/10.1016/j.isci.2019.100762

perovskite interfaces not only serve as encapsulants against the environment but also play multifunctional roles, acting as a semiconductor or charge tunneling layer, reducing charge-carrier recombination at the interface, and protecting the perovskite from degradation.

Similar interfacial passivation strategy has also been employed in other PV systems, such as quantum dots (QDs) solar cells. It is amazing that the perovskite materials can be used as a passivant in QD solar cells. Sargent et al. (Yang et al., 2015a) and Liang et al. (Peng et al., 2016) have used the $MAPbI_3$ perovskite to passivate inorganic PbS colloidal QDs itself and the interface of PbS QDs film, respectively. Significantly improved device performance has been achieved for inorganic PbS QDs solar cells. It was reported that the perovskite and PbS/PbSe can be well connected in their lattice fringes to form a heterocrystal, i.e., QDs-in-matrix, owing to the extremely minimal lattice mismatch (Ning et al., 2015; Yang et al., 2015b), which might be the reason for the improved device performance of PbS QDs solar cells. PbS QDs have also been employed as the hole transporter and co-sensitizer in PSCs (Li et al., 2015; Hu et al., 2015; Etgar et al., 2014); however, the performance is still not satisfactory. Besides PbS, numerous QDs, such as PbSe (Zhang et al., 2017), SnS (Han et al., 2017), CdSe (Qi et al., 2018), and $Cu(In,Ga)(S,Se)_2$ (Khanzada et al., 2016), have also been introduced into PSCs to be used as a dopant, passivant, interfacial layer, or charge transporting layer. The detailed PV performances are summarized in Table S1. These results indicate that the QDs exhibit great application potential in PV area. Recently, Lin and co-workers (Han et al., 2018) have fabricated a perovskite-QDs hybrid film (bulk heterojunction [BHJ]) by adding the PbS QDs into the perovskite precursor solution. Improved film quality combined with a PCE of 18.6% has been achieved due to the formation of QDs-in-perovskite structure. However, the BHJ structure has the drawback of uncontrolled distribution of QDs in the perovskite layer, which can lead to unfavorable contact between electron- and hole-extracting materials (Wu et al., 2016).

Here, we report an interfacial heterojunction engineering method to passivate the defects at the interface and GBs of MA-free perovskite. A modified green anti-solvent-assisted approach was adopted to fabricate the PbS QDs containing (Cs,FA)-based perovskite films (the formula of perovskite was $Cs_{0.15}FA_{0.85}Pb(I_{0.9}Br_{0.1})_3$) (Chen et al., 2018). The interfacial trap states have been well passivated by the PbS interfacial layer along with the significantly reduced non-radiation interfacial recombination, which is favorable for the charge-carrier transfer and collection. As a result, the device with PbS QDs passivation layer yielded an open-circuit voltage (V_{OC}) as high as 1.146 V and a PCE of 21.07% and showed excellent long-term ambient stability, demonstrating the effectiveness of defects passivation to achieve efficient and stable PSCs.

RESULTS AND DISCUSSION

The PbS QDs were synthesized according to a widely adopted hot-injection colloidal solution approach (Barkhouse et al., 2011). The crystal phase and morphology of the synthesized QDs were disclosed to be cubic structure with an average size of 3.35 nm by using X-ray diffraction (XRD) patterns and transmission electron microscopy, respectively (as shown in Figure S1). The PbS-passivated perovskite film was fabricated by using the PbS-containing green antisolvent (PbS/anisole), as shown in Figure 1A. Figures 1B, 1C, and S2 present the top-view scanning electron microscopic images of the perovskite films without and with PbS. The pristine perovskite film is fully covered without pinholes, and the average crystal size of the perovskite is 200–300 nm. After the introduction of PbS QDs, slightly enlarged perovskite crystal size can be found, indicating that the quality of perovskite film has been improved. Similar results can be reached by the XRD patterns, as shown in Figure 1D. Both perovskite films made without and with PbS in the anti-solvent show the same crystal structure without detectable impurities, except that the film with PbS exhibited significantly increased intensity of the diffraction peaks located at 14.06° and 28.31°, which were assigned to the (110) and (220) crystal planes, respectively, indicative of the better crystallinity and preferable crystal growth along (110) facet. These results indicated that existence of PbS can promote and control the crystallization of perovskite, which agrees well with the previously reported results (Han et al., 2018). The values of the root-mean-square roughness were identified to be 16.1 and 14.5 nm for the pristine and passivated films, respectively, by atomic force microscopy, as shown in Figure S3. It is notable that the smoother surface is usually indicative of higher film quality. However, the existence of small amount of PbS at the interface and grain does not change the light absorption properties of perovskite films (Figure 1E). Larger grains and smoother surface are beneficial for the improvement of PV performance.

Figure S4 shows the elemental mapping of the perovskite film after passivation. The result confirmed that element introduced by PbS QDs is uniformly distributed on the surface of the perovskite film. To gain

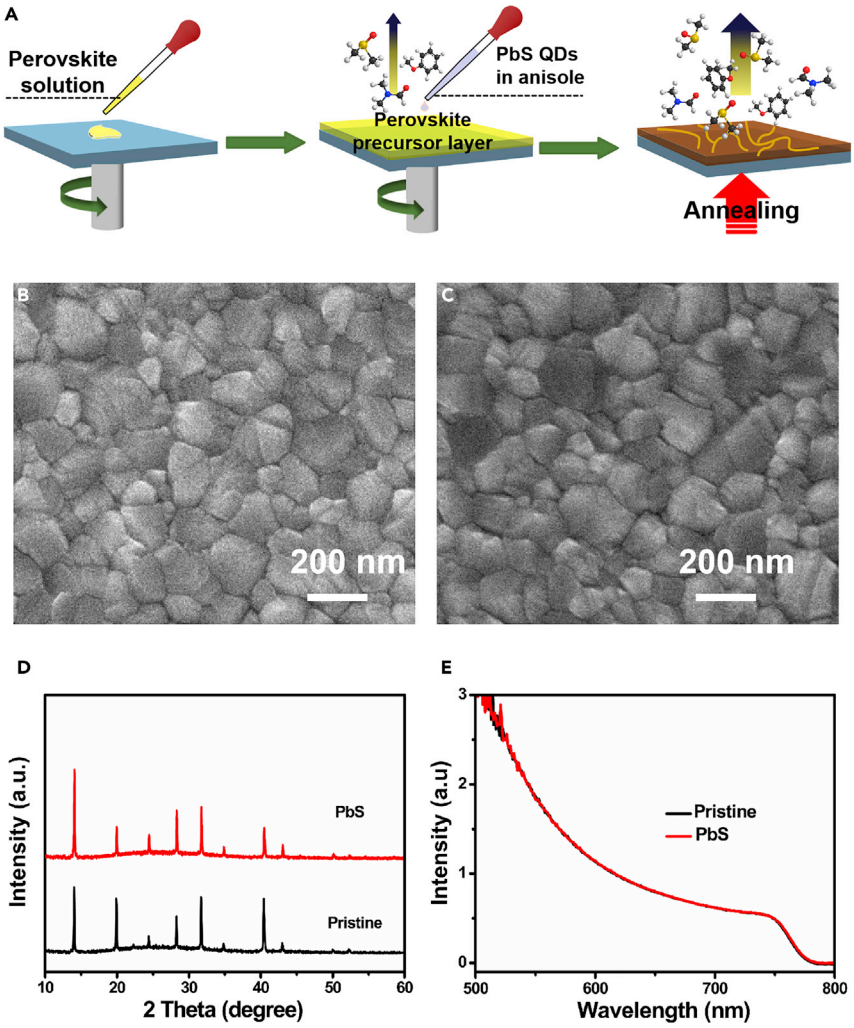

Figure 1. The Film Preparation Process and Characterization

(A–E) (A) Schematic illustration of the film preparation process; scanning electron microscopic images of the perovskite films without (B) and with PbS passivation layer (C); XRD patterns (D) and UV-visible absorption spectra (E) of the perovskite films with and without passivation layer.

insight into the distribution of PbS in the perovskite film, we then employed time-of-flight secondary-ion mass spectrometry to disclose the depth profile of PbS in the perovskite layer. In a negative mass detection mode, I^{127} and S^{32} were used as indicators of the perovskite and PbS, respectively. As shown in Figure 2A, a continuous and gradual increase with a significant spatial overlap on the I^{127} profile was revealed. In addition, the S^{32} depth profile shows a gradual decline in the very shallow perovskite layer (below 10 nm). These results demonstrate that a certain amount of PbS incorporated into the shallow perovskite with a gradient distribution near the interface; however, most of the PbS distributed at the perovskite surface. Given the fact that the synthesized PbS shows p-type character and higher the valence band maximum (VBM) (−5.1 eV) (Hyun et al., 2008) than perovskite, the interfacial carrier transfer and collection should be well improved.

We then fabricated planar perovskite devices to evaluate the efficacy of the passivation layer, the structure is FTO/c-TiO_2/perovskite/spiro-OMeTAD/Au (FTO: fluorine-doped tin oxide, spiro-OMeTAD: 2,2′,7,7′-tetrakis(*N*,*N*-dipmethoxyphenylamine)-9,9′-spirobifluorene). The thicknesses of the compact TiO_2, perovskite layer, and hole transporting layer (HTL) were about 30, 700, and 250 nm, respectively (Figure S5). The concentration of PbS in anisole was first investigated. As shown in Figure 2B, the device performance highly depends on the concentration of PbS. The average PCE was improved from 18.9% for the pristine device

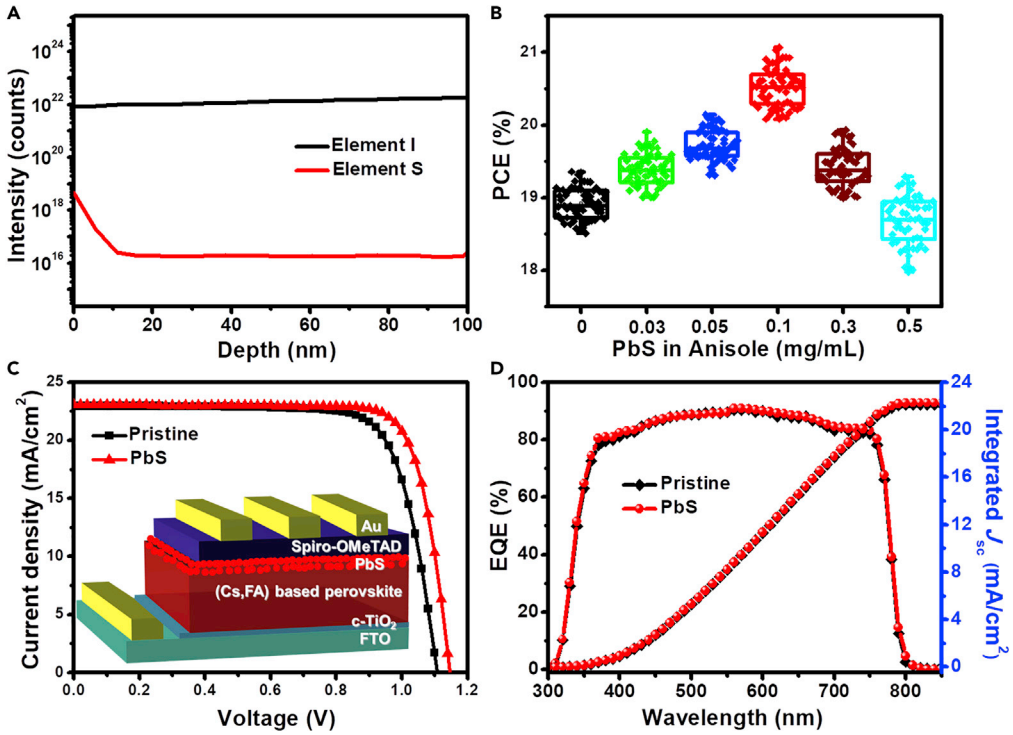

Figure 2. PSCs and their Photovoltaic Performance

(A) Secondary-ion mass spectrometry profiles from the top to the bottom of the PbS-passivated perovskite film. See also Figure S4.

(B) Statistics of the PCEs for devices with different concentration of PbS passivant.

(C) *J-V* curves of the devices based on the pristine and PbS-passivated perovskite (inset: the device architecture). See also Figure S6 and Table 1.

(D) External quantum efficiency curves and the corresponding integrated photocurrent for both devices.

to 20.5% for the passivated device with 0.1 mg/mL of PbS/anisole. Figure 2C presents the *J-V* characteristics of the best devices with and without PbS passivation layer under standard AM 1.5 illumination (at 100 mW cm^{-2}). The main PV parameters, including short-circuit current density (J_{SC}), V_{OC}, fill factor (FF), and PCE, are summarized in Table 1. The control device based on the pristine perovskite exhibits a PCE of 19.35% with J_{SC} = 22.93 mA cm^{-2}, V_{OC} = 1,109 mV, and FF = 76.47%, whereas the PCE for the champion device with PbS passivation layer jumped to 21.07% with J_{SC} = 23.06 mA cm^{-2}, V_{OC} = 1,146 mV, and FF = 79.82%. The improvement of the device efficiency is mainly attributed to the significantly enhanced *Voc* and FF for the passivated device. The enhancement of V_{OC} should be related to the reduced interfacial defects (Wu et al., 2018). High FF (>75%) usually means the absence of large carrier extraction/injection barrier for the interface between perovskite and hole transporting materials/electronic transporting materials (HTM/ETM) (Hou et al., 2017). The FFs of the present devices are between 76% and 80%, indicating that the interfacial passivation can effectively improve carrier transfer and collection. Moreover, a modified *J-V* hysteresis effect index (*HEI*) is defined (as shown in Figure S6 and Table 1) by the following equation (Rong et al., 2017):

$$\textit{Hysteresis effect index } (HEI) = \frac{J_{FR(0.8\ V_{OC})} - J_{RF(0.8\ V_{OC})}}{\left(J_{FR(0.8\ V_{OC})} + J_{RF(0.8\ V_{OC})}\right)/2}$$

where $J_{FR(0.8Voc)}$ and $J_{RF(0.8Voc)}$ represent the current density at 80% of V_{OC} for F-R and R-F scans. The resulting *HEI* of 1.65% for the PbS QDs-passivated devices is much lower than that of the pristine one (11.26%), which indicated that the hysteresis can be effectively suppressed with PbS QDs as the interfacial layer.

The integrated photocurrent densities are calculated to be 22.13 and 22.29 mA cm^{-2} from the corresponding external quantum efficiency spectra for the control and passivated devices (Figure 2D), respectively, which are comparable to the J_{SC} values extracted from the corresponding *J-V* curves. Steady-state output

	Scan direction	V_{OC} (mV)	J_{SC} (mA cm^{-2})	FF (%)	PCE (%)	HEI (%)	R_s (Ω cm^2)	R_{sh} (Ω cm^2)
Pristine	Reverse	1,109	22.93	76.47	19.35	11.26	5.29	2,413.8
	Forward	1,075	22.97	70.01	17.21			
PbS	Reverse	1,146	23.06	79.82	21.07	1.65	4.29	4,186.1
	Forward	1,124	23.07	77.55	20.07			

Table 1. The Key Photovoltaic Parameters of the PSCs with and without Passivation Layer

efficiency measured at the maximum power point voltage (V_{mpp}) was then studied to accurately assess the performance of the device with and without passivation layer, as shown in Figure S7. The PCE of the PbS-passivated device stabilizes at 20.3% (V_{mpp} = 0.96 V), which is among the highest efficiency reported till date for the (Cs,FA)-based perovskite. In contrast, the control device presents a steady output efficiency of 18.1% (V_{mpp} = 0.92 V). These results demonstrate the superiority of the interfacial contact passivation in achieving high-efficiency PSC devices with high V_{OC}. To assess the reproducibility of our devices, 60 individual cells for the control and passivated devices were fabricated and the detailed parameters are shown in Figures 3A–3D. It is clear that all the key *J-V* parameters of the passivated device are better, and the corresponding distributions are narrower when compared with the control ones, confirming the reliability of our method to fabricate high-efficiency PSCs.

To understand the large enhancement of the PV performance, the trap density of states (tDOS) was measured to analyze the passivation effect of PbS QDs by using the thermal admittance spectroscopy (TAS), which has been widely used to determine the trap states in thin-film (Cu-In-Ga-Se) and organic solar cells (Boix et al., 2009; Walter et al., 1996). The density of shallower trap states (0.30–0.40 eV) was assigned to the trap at the GB and that of the deeper trap states (0.40–0.50 eV) was identified to the defects at the film surface (Zheng et al., 2017). As shown in Figure 4A, the device with PbS passivation layer had lower tDOS almost over the whole trap depth region, indicating that both GB and interfacial defects for the perovskite films were effectively passivated by PbS. It is reported that the V_{OC} of solar cells is strongly related to the recombination of defects in the bulk or on the surface of the absorber layer (Wetzelaer et al., 2015; Buin et al., 2014). Therefore the lower trap states should be responsible for the higher V_{OC} (1.146 V) for the passivated device in the present work. To deeply understand the reason of the defects passivation, the defect activation energy (E_a) was measured by TAS accordingly. The relationship between E_a and ω_0 follows the equation: $\omega_0 = \beta T^2 \exp(-E_a/kT)$, where the characteristic transition angular frequency (ω_0) was extracted from the capacitance-frequency spectrum (as shown in Figures S8A and S8B). As reported (Chen et al., 2019b), E_a is approximately equal to the depth of the trap state energy (E_T) relative to the VBM energy level (E_{VBM}) of perovskite ($E_a = E_T - E_{VBM}$). The E_a values for the pristine and the PbS-passivated devices were calculated to be 0.2698 eV and 0.2329 eV, respectively, from the Arrhenius plot as shown in Figure S8C (which derived from the temperature-dependent capacitance-frequency spectra). This result indicated that the device with passivation layer has a lower trap state energy. In other words, there were fewer vacancies or interstitial traps for the passivated films. Therefore the performance of the modified device has been effectively improved by PbS passivation, especially in terms of the V_{OC}. We further tested the dark *J-V* curves for both devices to understand the recombination mechanism in the devices (Figure S9A). It is well known that less defect in the perovskite film can decrease the recombination process and the corresponding dark saturation current density (J_0) of the device (Zhang et al., 2018). J_0 is an extremely important parameter and is traditionally used as an indicator of the recombination in a device. The values of J_0 can be extracted from the linear fit for the semi-logarithmic plot in a range near V_{OC} from the dark *J-V* plots (Figure S9B). The J_0 decreased from 3.86×10^{-8} mA/cm^2 for the control device to 5.25×10^{-9} mA/cm^2 for the device with passivation layer, indicative of a considerably lower recombination rate (Lv et al., 2018). Owing to this the V_{OC} increases on decreasing the value of J_0; significantly enhanced V_{OC} (from 1.109 to 1.146 V) was achieved for the passivated device in the present work. The ideality factor (*n*) is also an important parameter to reflect the trap-assisted recombination and is commonly used to describe the dependence of applied light intensity and voltage, which can be derived from the relationship of the light intensity versus V_{OC} (as shown in Figure 4B) (Bernechea et al., 2016). The *n* decreased from 1.80 for the pristine device to 1.53 for the passivated device, indicating that the trap-assisted (non-radiation) recombination process was suppressed due to the reduction of the interfacial and GB defect states of the perovskite film (Yang et al., 2016), which agrees well with the results of TAS.

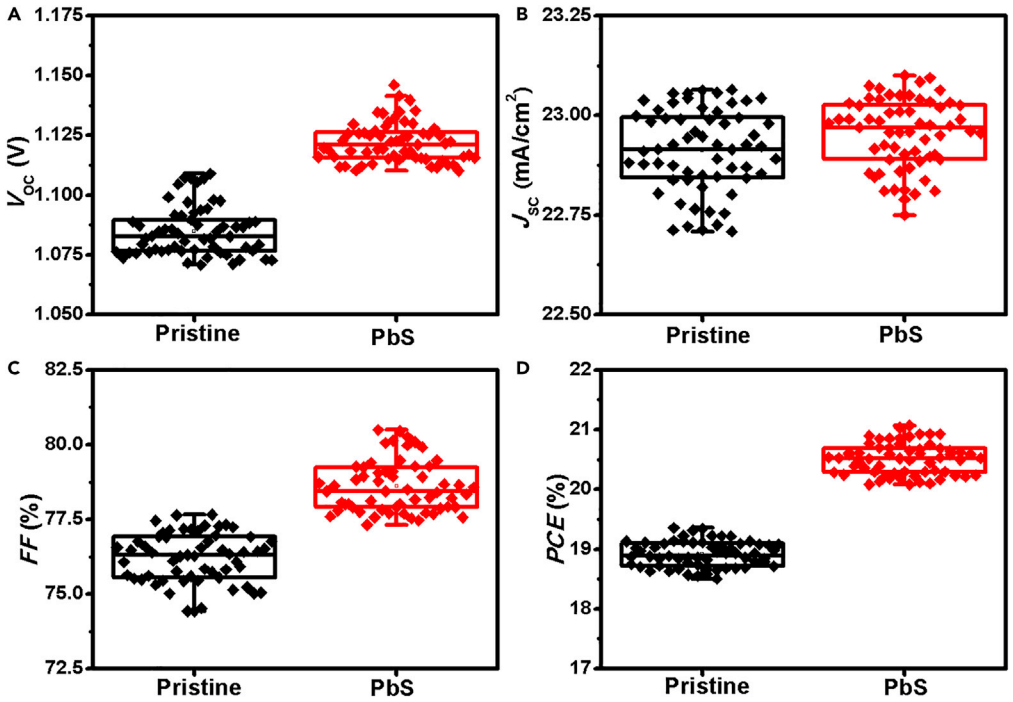

Figure 3. Statistics of PV Parameters

(A–D) Statistics of PV parameters for the devices based on the pristine and PbS-passivated perovskites: (A) J_{SC}, (B) V_{OC}, (C) FF, and (D) PCE.

PL spectroscopy is an important means to disclose the interfacial charge carrier transfer and extraction. Figure S10 shows that the HTM (spiro-OMeTAD) can quench the PL of the passivated perovskite film more effectively than the pristine perovskite film, which could be ascribed to the efficient charge transfer at the interface between HTM and perovskite (Tan et al., 2019). Similar results were further provided by the time-resolved PL spectroscopy (shown in Figure 4C). The fitted data are summarized in Table S2. The average PL life time (τ_{ave}) for the pristine perovskite sample is 368.1 ns, indicative of its high-quality film (Zheng et al., 2017; Yang et al., 2017; Wu et al., 2017). The average PL decay time is reduced to 20.97 ns upon introducing an HTL, indicating that the HTL can effectively extract the holes from the perovskite film. Moreover, PL decay time was further decreased to 9.44 ns for the sample with passivation layer, meaning that the holes transfer faster for the passivated sample than the control one, which should be attributed to the reduced interfacial trap state and the hole transfer ability of the passivant. Similar dual function effect has been achieved for the device passivated with the PTAA (poly[bis(4-phenyl)(2,4,6-trimethylphenyl) amine]) and poly-TPD (poly(4-butylphenyldiphenylamine)) (Wu et al., 2018; Tan et al., 2019). It is known that the reduced PL decay time is beneficial for suppressing the charge recombination at the interface and for improving device performance effectively. We then carried out electrochemical impedance spectroscopy to study the interfacial carrier transfer and transport kinetics. Figure 4D shows the Nyquist plots of the control and target devices. The arcs at high frequency were ascribed to carrier transport features in bulk layer and the incomplete semicircles in low frequency represent carrier recombination process at interfaces (Zhang et al., 2018; Yang et al., 2016). The corresponding values of R_{tr} (transport resistance) and R_{rec} (recombination resistance) were fitted by the Z-view software with the given equivalent circuit and summarized in Table S3. The device with passivation layer displays a lower R_{tr} and higher R_{rec} compared with the pristine one, indicating that a faster charge-carrier transfer and lower recombination rate is obtained for the passivated device, in good agreement with the previous results.

The stability of PSCs in ambient conditions is challenged by their sensitivity to moisture and oxygen due to the hygroscopic nature of the perovskite films. We thus evaluated the stability of both devices under ambient conditions at room temperature and relative humidity of 40%–70%. Figure 5A and Table S4 show the main parameters for the unencapsulated control and passivated devices. The PCE retains more than 93% of its initial efficiency even after 1 year's storage under the ambient conditions for both

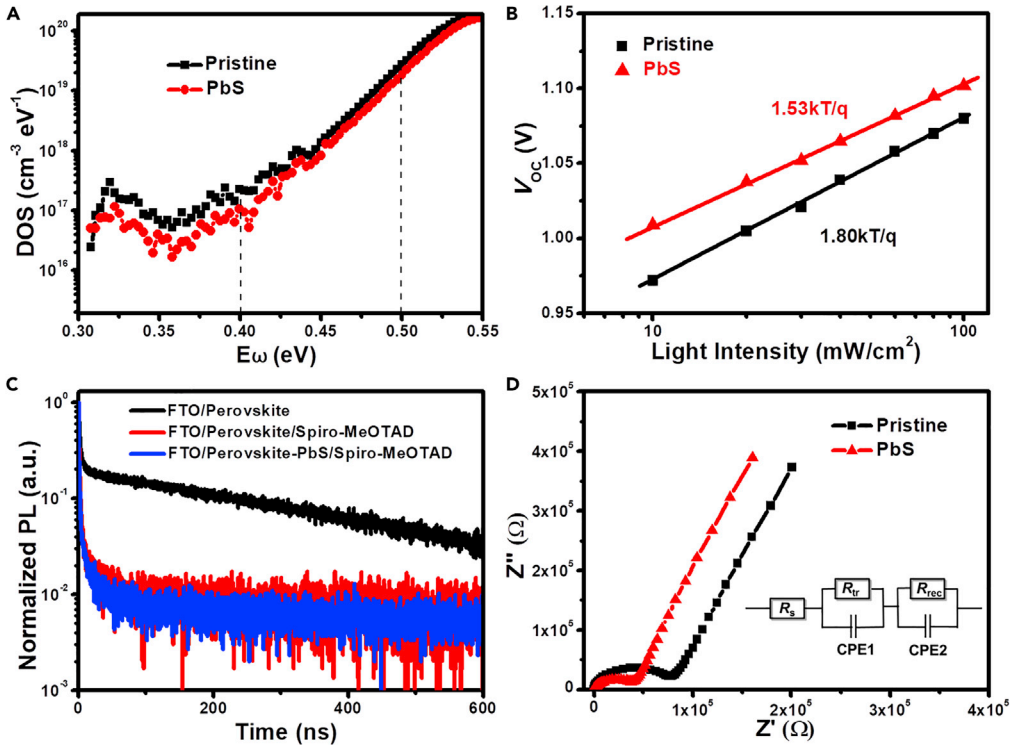

Figure 4. Dynamics Analysis of the Devices

(A) Trap density in pristine and PbS-passivated perovskite.

(B) V_{OC} versus light intensity for the control and passivated devices.

(C) TRPL decay profiles of the perovskites with and without passivation layer.

(D) Electrochemical impedance spectroscopy spectra for the devices based on the pristine and passivated perovskites.

devices. To obtain an in-depth understanding of the reasons for stability enhancement, the surface water contact angle (CA) of perovskite film was measured accordingly, as shown in Figure 5B. The CA for PbS-passivated perovskite film was 68.3°, much larger than 55.1° for the pristine film, indicating that the passivated film exhibits better hydrophobicity. This result is in good agreement with recently reported results that the increased CA was beneficial for inhibiting moisture penetration into the film and enhancing the overall device stability in humid environments (Li et al., 2016). Moreover, we further evaluated the thermal stability of the devices without and with the passivation layer by replacing the spiro-OMeTAD with PTAA. As shown in Figure 5C, more than 82% of its initial efficiency can be retained even after 1,000 hours of thermal aging at 85°C, demonstrating its superior thermal stability. The excellent stability of the present PSCs could be attributed to two factors: (1) the highly stable system of (Cs,FA) double-cation perovskite adopted in this work when compared with the MA-containing perovskites (Lee et al., 2015; Zheng et al., 2019; Park and Seok, 2019) and (2) the hydrophobicity of the perovskite film surface derived from PbS QDs.

Finally, to verify the universality of our interfacial contact passivation approach, perovskites with different component have been studied (as shown in Figure S11 and Table S5). It is clear that all the key *J-V* parameters for the PbS QD-passivated PSCs are better than those for the pristine one independent of the perovskite component. The significantly improved device performance should be attributed to the more superior carrier transport performance and the reduced non-radiation interfacial recombination after PbS passivation. These results demonstrated the effectiveness of interfacial contact passivation by using QDs in achieving highly efficient PSCs.

Conclusion

In summary, we have developed a universal interfacial contact passivation strategy to improve both efficiency and stability of planar PSCs by introducing a semiconductor passivation layer. The interfacial charge-carrier transfer was significantly improved due to the reduced trap states and suppressed non-

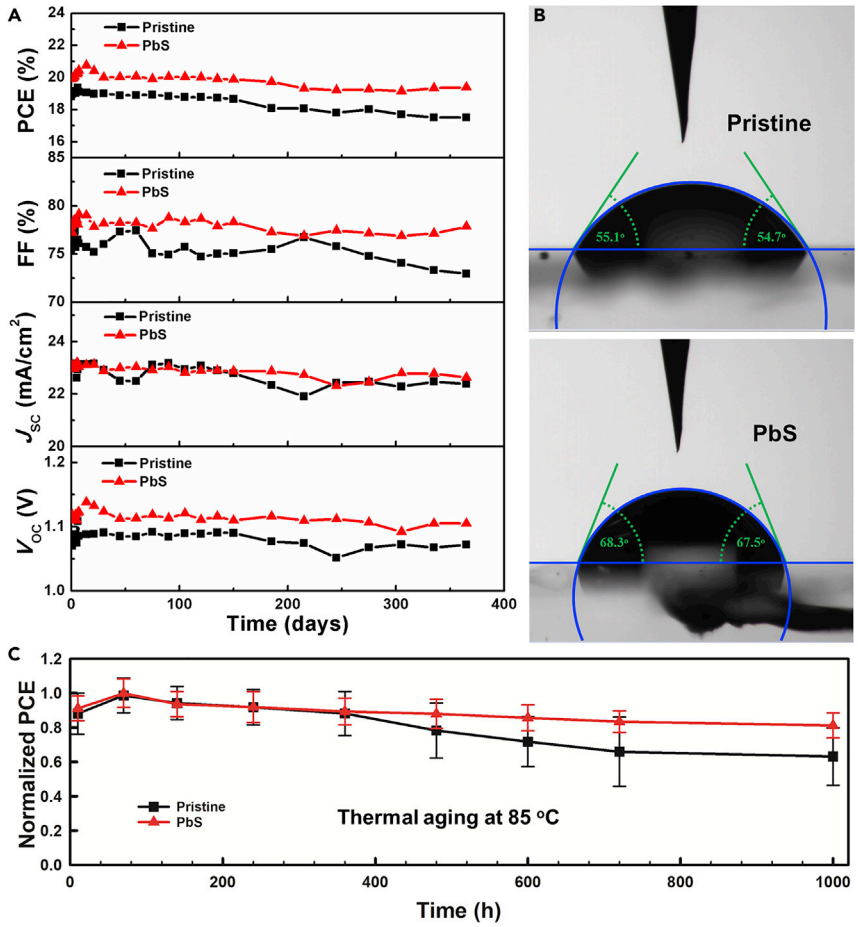

Figure 5. Stability of the Perovskite Solar Cells

(A) Long-term stability of the unsealed devices based on the pristine and PbS-passivated perovskite stored in dark under ambient conditions with humidity of 40%–70%.

(B) The water contact angle on the perovskite films with and without the PbS passivation layer.

(C) Normalized efficiencies of the pristine and the PbS-passivated PSCs under continuous heating at 85°C in N_2-filled glove box.

radiation recombination at the interface of HTL/perovskite, resulting in a V_{OC} of 1.146 V and a stabilized efficiency of 20.3%. Moreover, the (Cs,FA) double-cation perovskite-based device exhibits excellent long-term ambient and thermal stability, showing great application promise for the future mass production of PSCs.

Limitations of the Study

In this work, we introduced PbS QDs into the PSCs to *in situ* passivate the interfacial defects between perovskite and hole transporting layer. The optimal device shows excellent PCE with great long-term stability compared with the control one due to the reduced non-radiative recombination. However, the devices with PbS passivation layer show decreased device performance when the concentration of PbS exceeds 0.1 mg/mL. It would be more interesting if the crystallization process of perovskite films were studied through the grazing incidence wide-angle X-ray scattering measurement, to further investigate the effects of PbS-like QDs on the crystal orientations of MA-free, cesium/FA-double-cation-based perovskite films.

METHODS

All methods can be found in the accompanying Transparent Methods supplemental file.

SUPPLEMENTAL INFORMATION

Supplemental Information can be found online at https://doi.org/10.1016/j.isci.2019.100762.

ACKNOWLEDGMENTS

The authors thank the support from the National Natural Science Foundation of China (Grant No. 61904166 and 21773218), key research and development projects of Sichuan province (Grant No.2017GZ0052), Anshan Hifichem Co. Ltd, and the Jiangsu Province Cultivation base for State Key Laboratory of Photovoltaic Science and Technology.

AUTHOR CONTRIBUTIONS

Y.W. conceived the idea and designed the experiment. Y.C. and J.Y. conducted the synthesis and characterization experiments. S.W. conducted the PL and time-resolved PL experiments. Y.C. and J.Y. fabricated the devices and performed the PSC stability testing. Y.W. wrote the manuscript with comments and contributions from the other co-authors. Y.W., N.Y., and W.-H.Z. supervised the whole project.

DECLARATION OF INTERESTS

The authors declare no competing financial interest.

Received: July 8, 2019
Revised: October 17, 2019
Accepted: December 5, 2019
Published: January 24, 2020

REFERENCES

Barkhouse, D.A.R., Debnath, R., Kramer, I.J., Zhitomirsky, D., Pattantyus-Abraham, A.G., Levina, L., Etgar, L., Grätzel, M., and Sargent, E.H. (2011). Depleted bulk heterojunction colloidal quantum dot photovoltaics. Adv. Mater. *23*, 3134–3138.

Bernechea, M., Miller, N.C., Xercavins, G., So, D., Stavrinadis, A., and Konstantatos, G. (2016). Solution-processed solar cells based on environmentally friendly $AgBiS_2$ nanocrystals. Nat. Photon. *10*, 521.

Boix, P.P., Garcia-Belmonte, G., Muñecas, U., Neophytou, M., Waldauf, C., and Pacios, R. (2009). Determination of gap defect states in organic bulk heterojunction solar cells from capacitance measurements. Appl. Phys. Lett. *95*, 233302.

Brenner, T.M., Egger, D.A., Kronik, L., Hodes, G., and Cahen, D. (2016). Hybrid organic—inorganic perovskites: low-cost semiconductors with intriguing charge-transport properties. Nat. Rev. Mater. *1*, 15007.

Buin, A., Pietsch, P., Xu, J., Voznyy, O., Ip, A.H., Comin, R., and Sargent, E.H. (2014). Materials processing routes to trap-free halide perovskites. Nano Lett. *14*, 6281–6286.

Chen, Y., Yang, Z., Wang, S., Zheng, X., Wu, Y., Yuan, N., Zhang, W.-H., and Liu, S. (2018). Design of an inorganic mesoporous hole-transporting layer for highly efficient and stable inverted perovskite solar cells. Adv. Mater. *30*, 1805660.

Chen, Y., Yang, Z., Jia, X., Wu, Y., Yuan, N., Ding, J., Zhang, W.-H., and Liu, S. (2019a). Thermally stable methylammonium-free inverted perovskite solar cells with Zn^{2+} doped $CuGaO_2$ as efficient mesoporous hole-transporting layer. Nano Energy *61*, 148–157.

Chen, Y., Li, N., Wang, L., Li, L., Xu, Z., Jiao, H., Liu, P., Zhu, C., Zai, H., Sun, M., et al. (2019b). Impacts of alkaline on the defects property and crystallization kinetics in perovskite solar cells. Nat. Commun. *10*, 1112.

Cho, K.T., Paek, S., Grancini, G., Roldán-Carmona, C., Gao, P., Lee, Y., and Nazeeruddin, M.K. (2017). Highly efficient perovskite solar cells with a compositionally engineered perovskite/hole transporting material interface. Energy Environ. Sci. *10*, 621–627.

Cho, K.T., Grancini, G., Lee, Y., Oveisi, E., Ryu, J., Almora, O., Tschumi, M., Schouwink, P.A., Seo, G., Heo, S., et al. (2018). Selective growth of layered perovskites for stable and efficient photovoltaics. Energy Environ. Sci. *11*, 952–959.

Etgar, L., Gao, P., Qin, P., Graetzel, M., and Nazeeruddin, M.K. (2014). A hybrid lead iodide perovskite and lead sulfide QD heterojunction solar cell to obtain a panchromatic response. J. Mater. Chem. A *2*, 11586–11590.

Han, J., Yin, X., Nan, H., Zhou, Y., Yao, Z., Li, J., Oron, D., and Lin, H. (2017). Enhancing the performance of perovskite solar cells by hybridizing SnS quantum dots with $CH_3NH_3PbI_3$. Small *13*, 1700953.

Han, J., Luo, S., Yin, X., Zhou, Y., Nan, H., Li, J., Li, X., Oron, D., Shen, H., and Lin, H. (2018). Hybrid PbS quantum-dot-in-perovskite for high-efficiency perovskite solar cell. Small *14*, 1801016.

Hou, Y., Du, X., Scheiner, S., McMeekin, D.P., Wang, Z., Li, N., Killian, M.S., Chen, H., Richter, M., Levchuk, I., et al. (2017). A generic interface to reduce the efficiency-stability-cost gap of perovskite solar cells. Science *358*, 1192–1197.

Hu, L., Wang, W., Liu, H., Peng, J., Cao, H., Shao, G., Xia, Z., Ma, W., and Tang, J. (2015). PbS colloidal quantum dots as an effective hole transporter for planar heterojunction perovskite solar cells. J. Mater. Chem. A *3*, 515–518.

Hyun, B.-R., Zhong, Y.-W., Bartnik, A.C., Sun, L., Abruña, H.D., Wise, F.W., Goodreau, J.D., Matthews, J.R., Leslie, T.M., and Borrelli, N.F. (2008). Electron injection from colloidal PbS quantum dots into titanium dioxide nanoparticles. ACS Nano *2*, 2206–2212.

Jiang, Q., Zhao, Y., Zhang, X., Yang, X., Chen, Y., Chu, Z., Ye, Q., Li, X., Yin, Z., and You, J. (2019). Surface passivation of perovskite film for efficient solar cells. Nat. Photon. *13*, 460–466.

Khanzada, L.S., Levchuk, I., Hou, Y., Azimi, H., Osvet, A., Ahmad, R., Brandl, M., Herre, P., Distaso, M., Hock, R., et al. (2016). Effective ligand engineering of the Cu_2ZnSnS_4 nanocrystal surface for increasing hole transport efficiency in perovskite solar cells. Adv. Funct. Mater. *26*, 8300–8306.

Kojima, A., Teshima, K., Shirai, Y., and Miyasaka, T. (2009). Organometal halide perovskites as visible-light sensitizers for photovoltaic cells. J. Am. Chem. Soc. *131*, 6050–6051.

Lee, J.-W., Kim, D.-H., Kim, H.-S., Seo, S.-W., Cho, S.M., and Park, N.-G. (2015). Formamidinium and cesium hybridization for photo- and moisture-stable perovskite solar cell. Adv. Energy Mater. *5*, 1501310.

Li, Y., Zhu, J., Huang, Y., Wei, J., Liu, F., Shao, Z., Hu, L., Chen, S., Yang, S., Tang, J., et al. (2015).

Efficient inorganic solid solar cells composed of perovskite and PbS quantum dots. Nanoscale *7*, 9902–9907.

Li, Z., Yang, M., Park, J.-S., Wei, S.-H., Berry, J.J., and Zhu, K. (2016). Stabilizing perovskite structures by tuning tolerance factor: formation of formamidinium and cesium lead iodide solid-state alloys. Chem. Mater. *28*, 284–292.

Lin, Y., Shen, L., Dai, J., Deng, Y., Wu, Y., Bai, Y., Zheng, X., Wang, J., Fang, Y., Wei, H., et al. (2017). π-Conjugated Lewis base: efficient trap-passivation and charge-extraction for hybrid perovskite solar cells. Adv. Mater. *29*, 1604545.

Liu, L., Huang, S., Lu, Y., Liu, P., Zhao, Y., Shi, C., Zhang, S., Wu, J., Zhong, H., Sui, M., et al. (2018). Grain-boundary "patches" by in situ conversion to enhance perovskite solar cells stability. Adv. Mater. *30*, 1800544.

Lv, Y., Wang, P., Cai, B., Ma, Q., Zheng, X., Wu, Y., Jiang, Q., Liu, J., and Zhang, W.-H. (2018). Facile fabrication of SnO_2 nanorod arrays films as electron transporting layer for perovskite solar cells. Solar RRL *2*, 1800133.

Ning, Z., Gong, X., Comin, R., Walters, G., Fan, F., Voznyy, O., Yassitepe, E., Buin, A., Hoogland, S., and Sargent, E.H. (2015). Quantum-dot-in-perovskite solids. Nature *523*, 324.

Niu, T., Lu, J., Munir, R., Li, J., Barrit, D., Zhang, X., Hu, H., Yang, Z., Amassian, A., Zhao, K., et al. (2018). Stable high-performance perovskite solar cells via grain boundary passivation. Adv. Mater. *30*, 1706576.

NREL Chart (n.d.). Best research-cell efficiencies. https://www.nrel.gov/pv/assets/pdfs/best-reserch-cell-efficiencies.20190802.pdf.

Park, B.-w., and Seok, S.I. (2019). Intrinsic instability of inorganic–organic hybrid halide perovskite materials. Adv. Mater. *31*, 1805337.

Peng, J., Chen, Y., Zhang, X., Dong, A., and Liang, Z. (2016). Solid-state ligand-exchange fabrication of $CH_3NH_3PbI_3$ capped PbS quantum dot solar cells. Adv. Sci. *3*, 1500432.

Qi, J., Xiong, H., Wang, G., Xie, H., Jia, W., Zhang, Q., Li, Y., and Wang, H. (2018). High-performance solar cells with induced crystallization of perovskite by an evenly distributed CdSe quantum dots seed-mediated underlayer. J. Power Sources *376*, 46–54.

Qin, P.-L., Yang, G., Ren, Z.-w., Cheung, S.H., So, S.K., Chen, L., Hao, J., Hou, J., and Li, G. (2018). Stable and efficient organo-metal halide hybrid perovskite solar cells via π-conjugated Lewis base polymer induced trap passivation and charge extraction. Adv. Mater. *30*, 1706126.

Rong, Y., Hu, Y., Ravishankar, S., Liu, H., Hou, X., Sheng, Y., Mei, A., Wang, Q., Li, D., Xu, M., et al. (2017). Tunable hysteresis effect for perovskite solar cells. Energy Environ. Sci. *10*, 2383–2391.

Tan, F., Tan, H., Saidaminov, M.I., Wei, M., Liu, M., Mei, A., Li, P., Zhang, B., Tan, C.-S., Gong, X., et al. (2019). In situ back-contact passivation improves photovoltage and fill factor in perovskite solar cells. Adv. Mater. *31*, 1807435.

Turren-Cruz, S.-H., Hagfeldt, A., and Saliba, M. (2018). Methylammonium-free, high-performance, and stable perovskite solar cells on a planar architecture. Science *362*, 449–453.

Walter, T., Herberholz, R., Müller, C., and Schock, H.W. (1996). Determination of defect distributions from admittance measurements and application to $Cu(In,Ga)Se_2$ based heterojunctions. J. Appl. Phys. *80*, 4411–4420.

Wang, P., Wu, Y., Cai, B., Ma, Q., Zheng, X., and Zhang, W.-H. (2019). Solution-processable perovskite solar cells toward commercialization: progress and challenges. Adv. Funct. Mater. *0*, 1807661.

Wetzelaer, G.-J.A.H., Scheepers, M., Sempere, A.M., Momblona, C., Ávila, J., and Bolink, H.J. (2015). Trap-assisted non-radiative recombination in organic–inorganic perovskite solar cells. Adv. Mater. *27*, 1837–1841.

Wu, Y., Yang, X., Chen, W., Yue, Y., Cai, M., Xie, F., Bi, E., Islam, A., and Han, L. (2016). Perovskite solar cells with 18.21% efficiency and area over 1 cm^2 fabricated by heterojunction engineering. Nat. Energy *1*, 16148.

Wu, Y., Xie, F., Chen, H., Yang, X., Su, H., Cai, M., Zhou, Z., Noda, T., and Han, L. (2017). Thermally stable $MAPbI_3$ perovskite solar cells with efficiency of 19.19% and area over 1 cm^2 achieved by additive engineering. Adv. Mater. *29*, 1701073.

Wu, Y., Wang, P., Wang, S., Wang, Z., Cai, B., Zheng, X., Chen, Y., Yuan, N., Ding, J., and Zhang, W.-H. (2018). Heterojunction engineering for high efficiency cesium formamidinium double-cation lead halide perovskite solar cells. ChemSusChem. *11*, 837–842.

Yang, Z., Janmohamed, A., Lan, X., García de Arquer, F.P., Voznyy, O., Yassitepe, E., Kim, G.-H., Ning, Z., Gong, X., Comin, R., et al. (2015a). Colloidal quantum dot photovoltaics enhanced by perovskite shelling. Nano Lett. *15*, 7539–7543.

Yang, Z., Yassitepe, E., Voznyy, O., Janmohamed, A., Lan, X., Levina, L., Comin, R., and Sargent, E.H. (2015b). Self-assembled PbSe nanowire:perovskite hybrids. J. Am. Chem. Soc. *137*, 14869–14872.

Yang, D., Zhou, X., Yang, R., Yang, Z., Yu, W., Wang, X., Li, C., Liu, S., and Chang, R.P.H. (2016). Surface optimization to eliminate hysteresis for record efficiency planar perovskite solar cells. Energy Environ. Sci. *9*, 3071–3078.

Yang, W.S., Park, B.-W., Jung, E.H., Jeon, N.J., Kim, Y.C., Lee, D.U., Shin, S.S., Seo, J., Kim, E.K., Noh, J.H., et al. (2017). Iodide management in formamidinium-lead-halide–based perovskite layers for efficient solar cells. Science *356*, 1376–1379.

Yang, C., Wu, Y., Ma, Q., and Zhang, W.-H. (2018). Nanocrystals of halide perovskite: synthesis, properties, and applications. J. Energy Chem. *27*, 622–636.

Zhang, W., Eperon, G.E., and Snaith, H.J. (2016). Metal halide perovskites for energy applications. Nat. Energy *1*, 16048.

Zhang, Z., Chen, Z., Yuan, L., Chen, W., Yang, J., Wang, B., Wen, X., Zhang, J., Hu, L., Stride, J.A., et al. (2017). A new passivation route leading to over 8% efficient PbSe quantum-dot solar cells via direct ion exchange with perovskite nanocrystals. Adv. Mater. *29*, 1703214.

Zhang, M., Wang, Z., Zhou, B., Jia, X., Ma, Q., Yuan, N., Zheng, X., Ding, J., and Zhang, W.-H. (2018). Green anti-solvent processed planar perovskite solar cells with efficiency beyond 19%. Solar RRL *2*, 1700213.

Zheng, X., Chen, B., Dai, J., Fang, Y., Bai, Y., Lin, Y., Wei, H., Zeng, X., and Huang, J. (2017). Defect passivation in hybrid perovskite solar cells using quaternary ammonium halide anions and cations. Nat. Energy *2*, 17102.

Zheng, X., Deng, Y., Chen, B., Wei, H., Xiao, X., Fang, Y., Lin, Y., Yu, Z., Liu, Y., Wang, Q., et al. (2018). Dual functions of crystallization control and defect passivation enabled by Sulfonic zwitterions for stable and efficient perovskite solar cells. Adv. Mater. *30*, 1803428.

Zheng, X., Troughton, J., Gasparini, N., Lin, Y., Wei, M., Hou, Y., Liu, J., Song, K., Chen, Z., Yang, C., et al. (2019). Quantum dots supply bulk- and surface-passivation agents for efficient and stable perovskite solar cells. Joule *3*, 1963–1976.

iScience, Volume *23*

Supplemental Information

Interfacial Contact Passivation for Efficient and Stable Cesium-Formamidinium Double-Cation Lead Halide Perovskite Solar Cells

Yu Chen, Jianchao Yang, Shubo Wang, Yihui Wu, Ningyi Yuan, and Wen-Hua Zhang

Supporting Information

This PDF file includes:

Figure S1 to S11

Tables S1 to S5

Transparent Methods

Supplemental References

Figures：

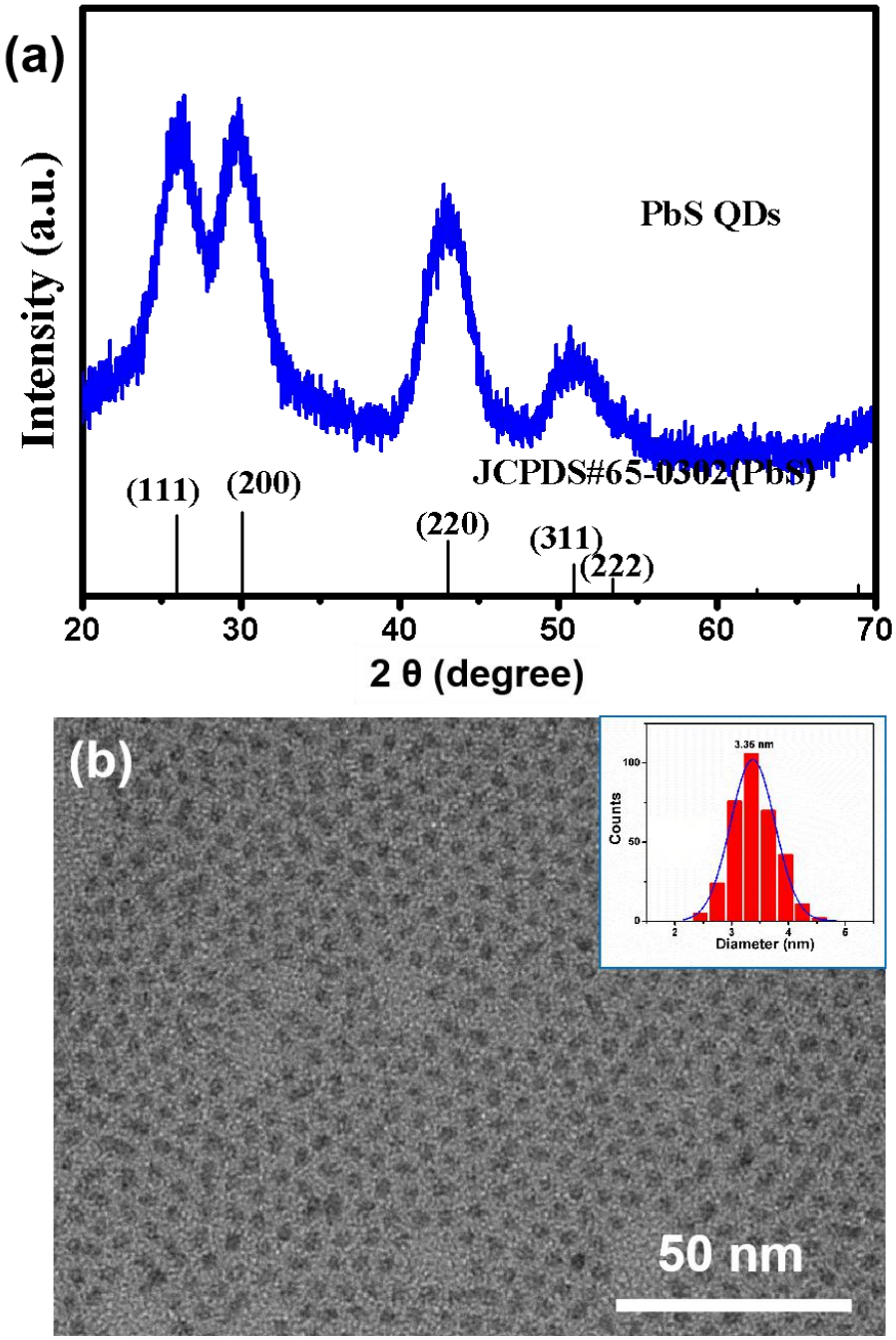

Figure S1. (a) XRD patterns and (b)TEM images of the PbS QDs (inset: partical size distribution), Related to Figure 1

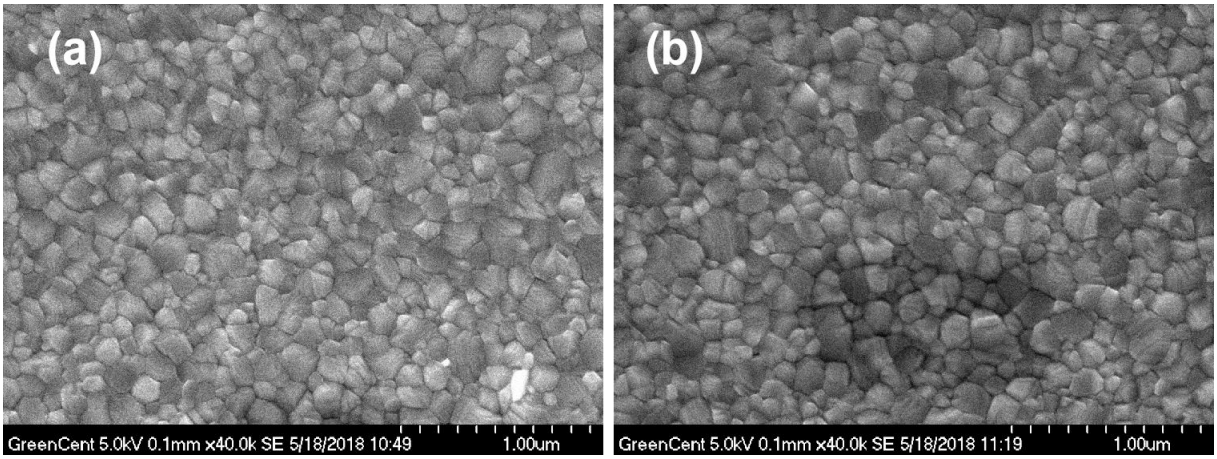

Figure S2. SEM images of the pristine (a) and PbS passivated (b) perovskite films, Related to Figure 1

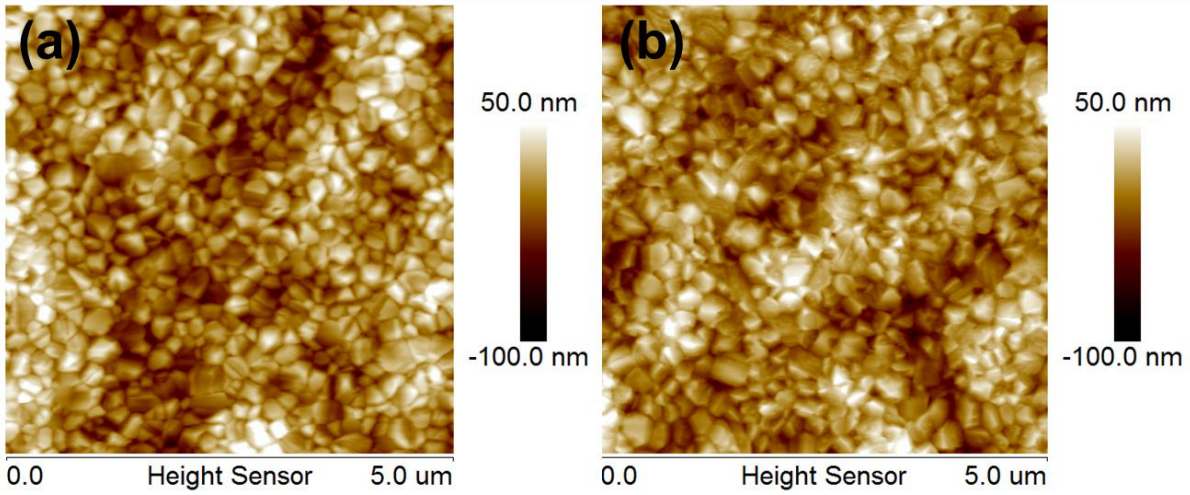

Figure S3. AFM images of the pristine (a) and PbS passivated (b) perovskite films, Related to Figure 1

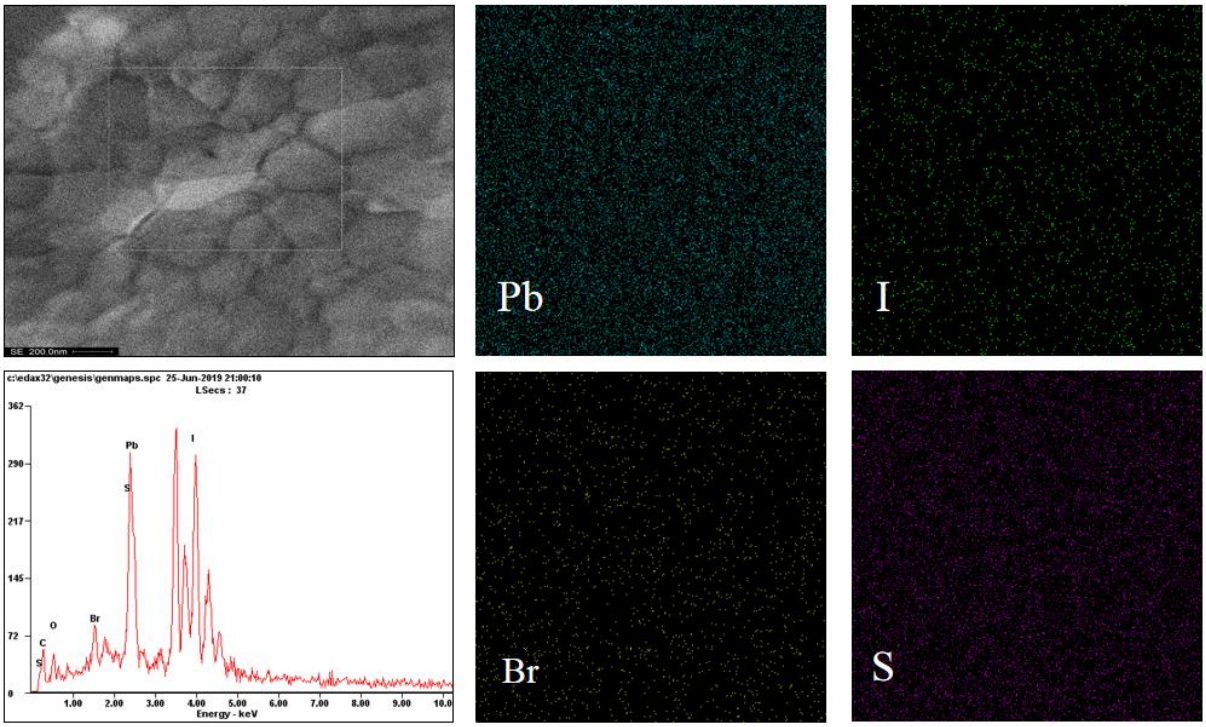

Figure S4. Elemental mapping of the passivated perovskite films, Related to Figure 2A

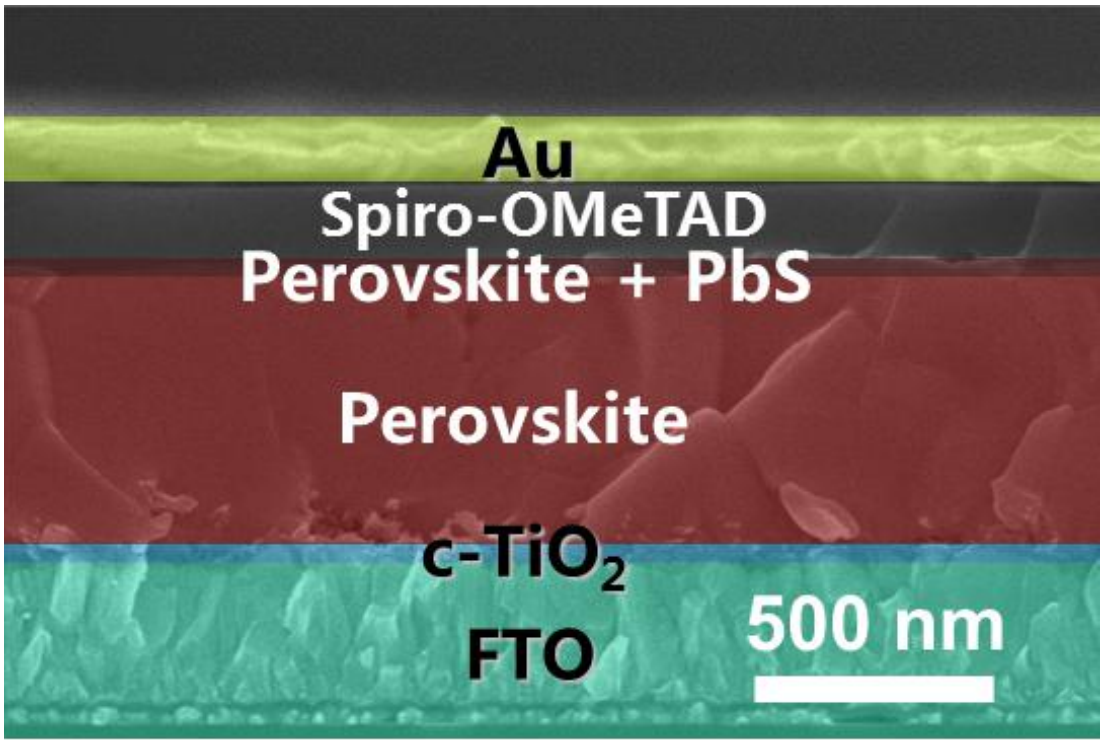

Figure S5. Typical cross-sectional SEM image of the passivated PSCs, Related to Figure 2C

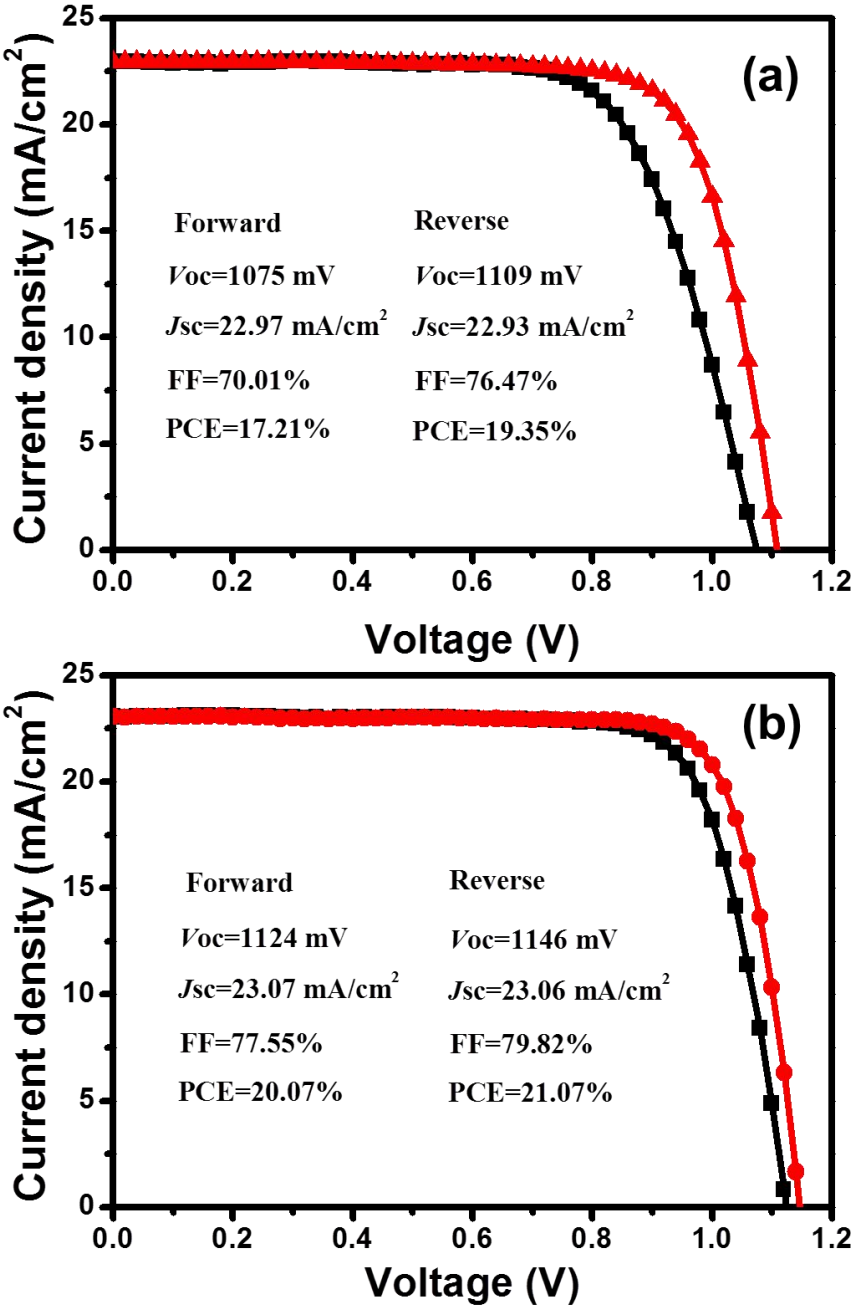

Figure S6. Hysteretic effect of the devices based on the pristine (a) and the passivated (b) perovskite films, Related to Figure 3 and Table 1

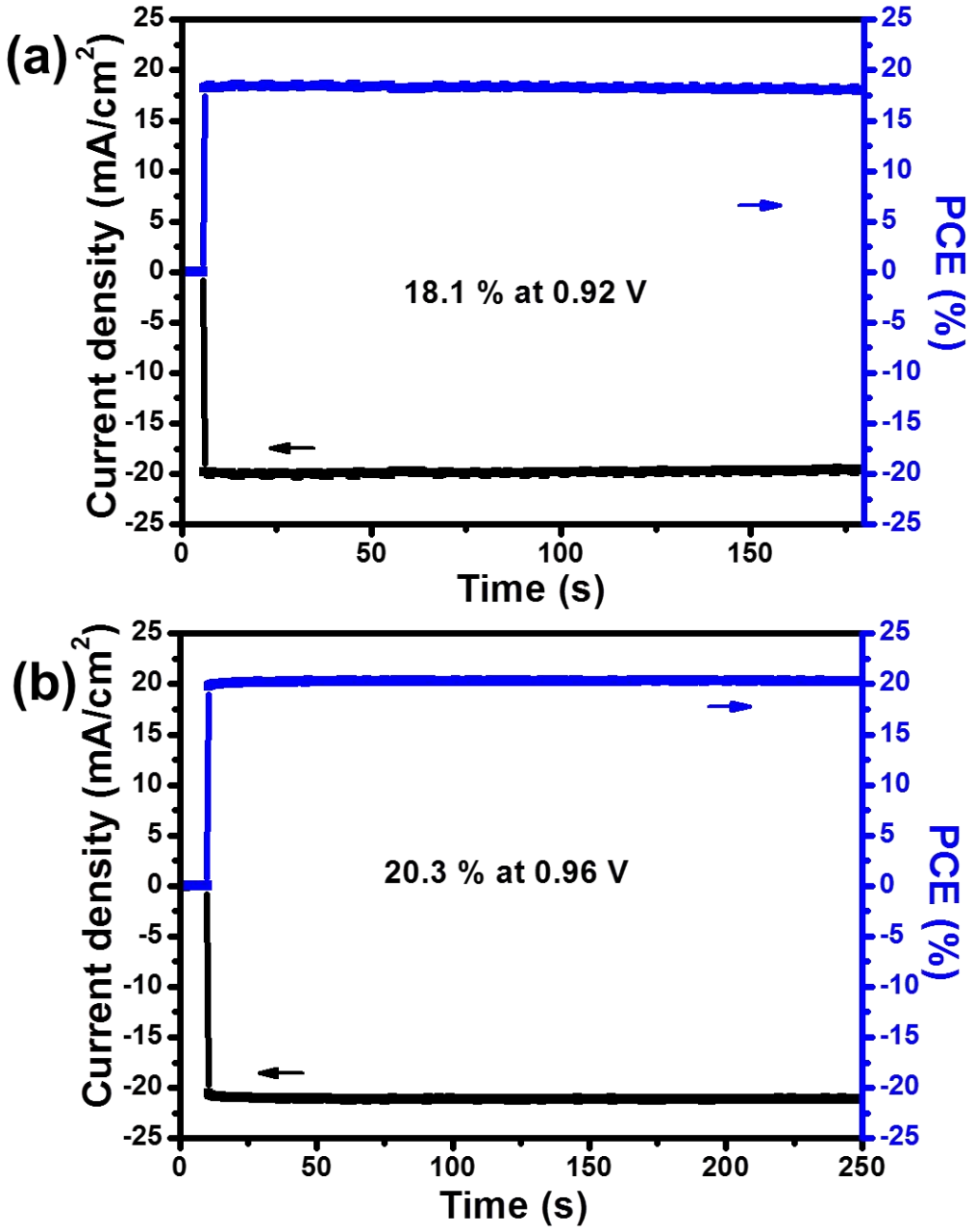

Figure S7. Stabilized output efficiency of the device based on the pristine (a) and the PbS passivated perovskite (b) around the maximum output power point a function of time under simulated 1 sun illumination, Related to Figure 3

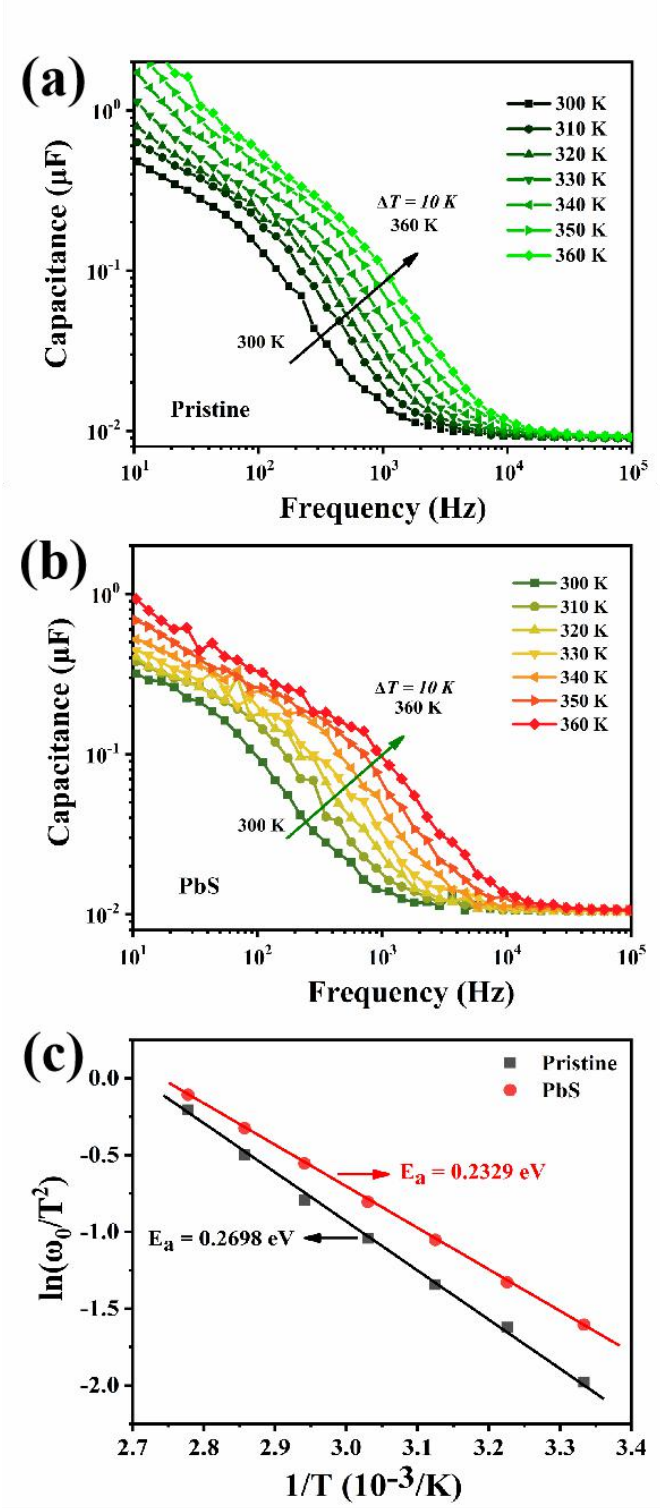

Figure S8. Admittance spectra of the reference PSC without (a) and with (b) PbS passivation layer, measured at a temperature between 300 and 360 K with a step of 10 K. (c) The corresponding Arrhenius plots derived from (a) and (b), Related to Figure 4

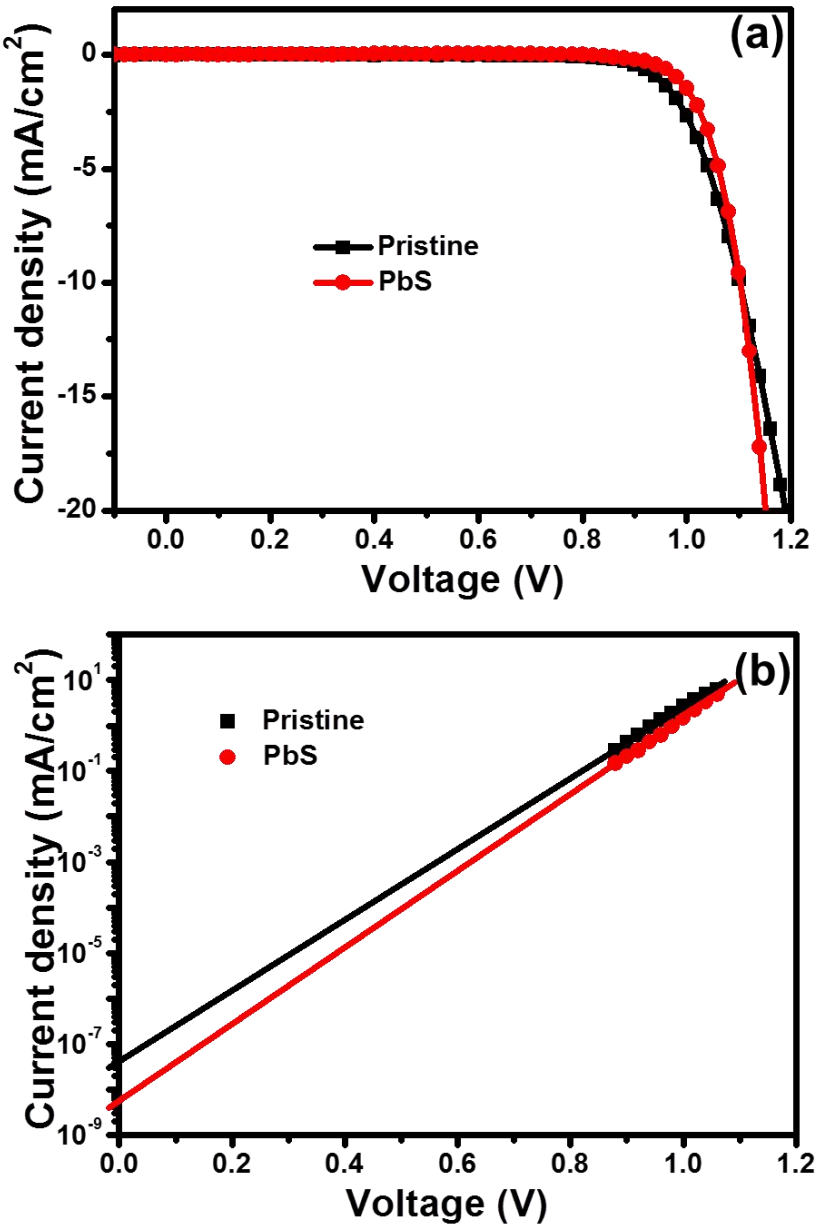

Figure S9. Dark J-V curves of the PSCs based on the pristine and the PbS passivated perovskite: a) linear plot and b) semi-logarithmic plot, Related to Figure 4

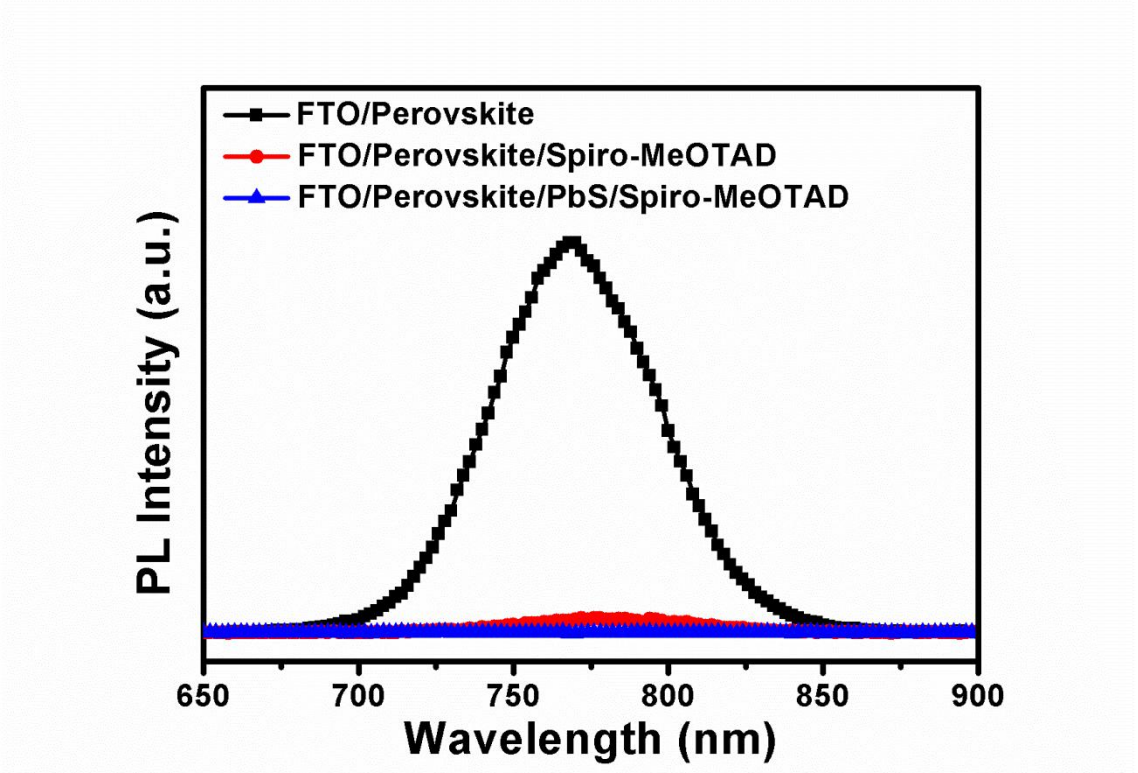

Figure S10. Steady PL spectra of the perovskite with and without the passivation layer, Related to Figure 4C

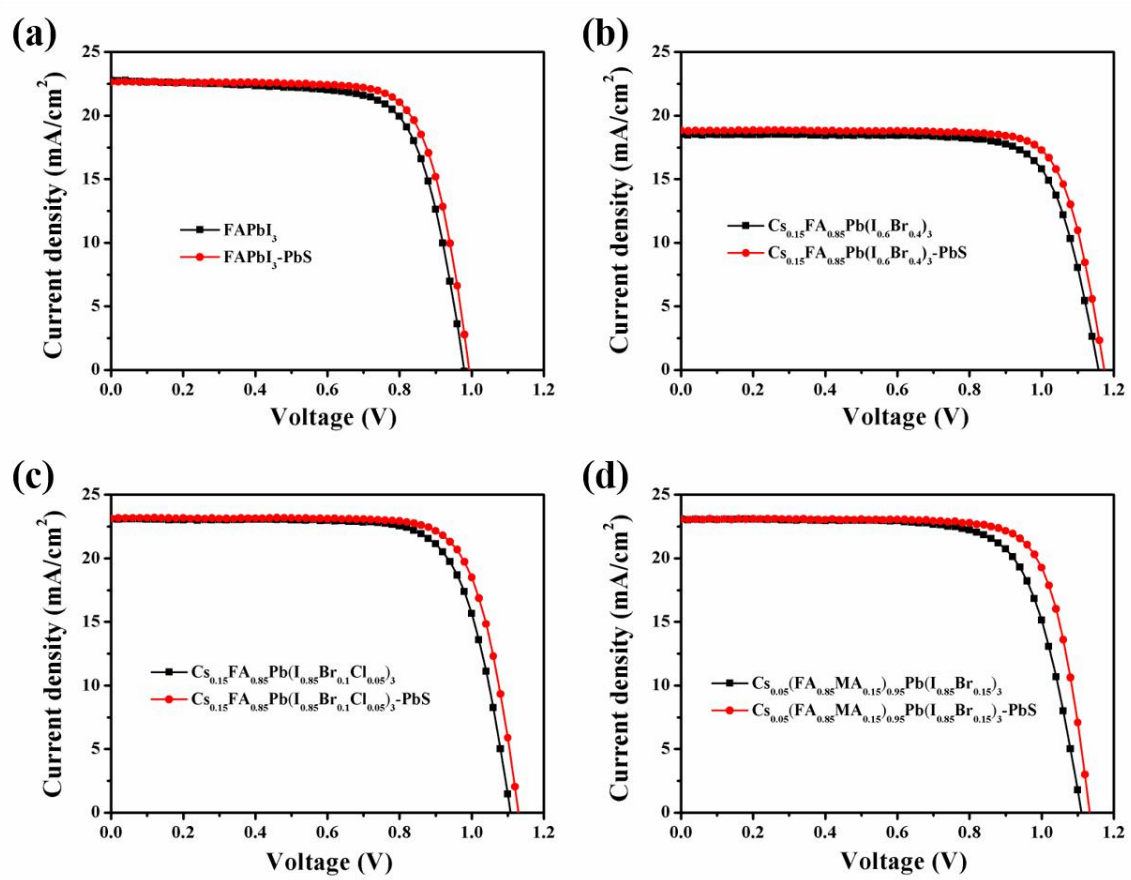

Figure S11. *J-V* curves of the devices with and without PbS passivation layer for different perovskite components, Related to Figure 4

Tables:

Table S1. Briefly summary on the recently development of Quantum dots materials, Related to Figure 4 and Table 1

Quantum Dots Materials	Devices Configurations	V_{oc} (V)	J_{sc} (mA/cm^2)	FF (%)	PCE (%)	Ref.
PbS	FTO/bl-TiO_2/mp-TiO_2/$CH_3NH_3PbI_3$/PbS-QDs/Au	0.34	24.63	0.43	3.60	(Etgar et al., 2014)
PbS	ITO/ZnO/PbS@$CH_3NH_3PbI_3$/PbS-EDT/Au	0.61	21.80	0.68	8.95	(Yang et al., 2015)
PbS	ITO/MgZnO/PbS@$CsPbI_3$/PbS@EDT/Au	0.64	24.50	0.67	10.5	(Zhang et al., 2018)
PbSe	FTO/bl-TiO_2/PbSe-QDs@$CsPbBr_3$/Au	0.53	25.10	0.62	8.20	(Zhang et al., 2017)
CdSe	FTO/bl-TiO_2/mp-TiO_2/CdSe/$CH_3NH_3PbI_3$/spiro-OMeTAD/Au	1.08	20.57	0.70	15.68	(Qi et al., 2018)
CdSe	ITO/PEDOT:PSS/$CH_3NH_3PbI_{3-x}Cl_x$/CdSe/PCBM/Rhodamine101/LiF/Ag	0.90	20.96	0.73	13.73	(Zeng et al., 2017)
CdS	FTO/TiO_2/CdS QDs/$CH_3NH_3PbI_3$/spiro-OMeTAD/Au	0.94	16.70	0.64	10.52	(Ali et al., 2018)
CdTe	ITO/SnO_2/$CH_3NH_3PbI_3$/CdTe-QD/Spiro-OMeTAD/Ag	1.10	22.42	0.78	19.19	(Xiao et al., 2018)
SnS	FTO/TiO_2/SnS-QDs@$MAPbI_3$/Spiro-OMeTAD/Au	1.04	22.70	0.72	16.80	(Han et al., 2017)
CIS	FTO/TiO_2/$CH_3NH_3PbI_3$/CIS/spiro-OMeTAD/Au	1.04	21.80	0.61	13.80	(Ma et al., 2017)
CZTS	ITO/CZTS/$CH_3NH_3PbI_3$/PCBM/PrCMA/Ag	0.92	20.70	0.81	15.40	(Khanzada et al., 2016)
Cu(In,Ga)(S,Se)$_2$	FTO/bl-TiO_2/mp-TiO_2/$CH_3NH_3PbI_3$/Cu(In,Ga)(S,Se)$_2$-QDs/Au	0.94	17.66	0.55	9.15	(Xu et al., 2017)
ZnO/rGO	FTO/ZnO@rGO/$CH_3NH_3PbI_3$/spiro-OMeTAD/Au	1.03	21.70	0.68	15.20	(Tavakoli et al., 2016)
SnO_2	FTO/TiO_2/SnO_2-QDs/ $CsMAFAPbI_3Br_{3-x}$/Spiro-OMeTAD/Au	1.11	20.70	0.75	17.30	(Wu et al., 2019)
TiO_2	FTO/TiO_2(QDs)/mp-TiO_2/$CH_3NH_3PbI_3$/spiro-OMeTAD/Au	1.06	22.48	0.71	16.97	(Tu et al., 2015)
$CsPbCl_3$:Mn	$CsPbCl_3$:Mn-QDs/FTO/TiOx/$CH_3NH_3PbI_3$/spiro-OMeTAD/Au	1.11	22.03	0.76	18.57	(Wang et al., 2017)
$CsPbBr_{1.85}I_{1.15}$	FTO/c-TiO_2/mp-TiO_2/$CsFAMAPb(I_{0.85}Br_{0.15})_3$ / $CsPbBr_{1.85}I_{1.15}$ -QDs/spiro-OMeTAD/Au	1.14	23.35	0.79	21.14	(Akin et al., 2019)
$CsPbBrCl_2$	FTO/PTAA/$CH_3NH_3PbI_3$/$CsPbBrCl_2$-QDs/C_{60}/BCP/Cu	1.15	23.40	0.80	21.50	(Zheng et al., 2019)
$CsPbI_3$	FTO/m-TiO_2/$FAMAPbI_3$/$CsPbI_3$ -QDs/Spiro-OMeTAD/Au	1.09	24.42	0.70	18.56	(Liu et al., 2018)

Table S2. Parameters of the TRPL spectroscopy based on different samples, Related to Figure 4C

samples	τ_{ave} (ns)	τ_1 (ns)	τ_2 (ns)	A_1	A_2
Glass/perovskite	368.1	2.50	376.6	0.690	0.197
Glass/perovskite/spiro-OMeTAD	20.97	1.29	47.31	0.932	0.019
Glass/perovskite-PbS/spiro-OMeTAD	9.44	0.96	22.26	0.981	0.028

Table S3. EIS parameters of the devices based on the pristine and the PbS passivated perovskite films, Related to Figure 4D

	R_s (Ω)	R_{tr} (Ω)	R_{rec} (Ω)	CPE1 (F)	CPE2 (F)
pristine	54.92	79201	745704	9.70E-9	1.047E-6
PbS	40.52	37425	864613	9.76E-9	0.999E-6

Table S4. Time evolution of the photovoltaic parameters for PSCs with and without PbS passivation, Related to Figure 5

	Time (days)	V_{OC} (V)	J_{SC} (mA cm^{-2})	*FF*(%)	*PCE* (%)
Pristine	0	1.08	23.16	75.45	18.83
	1	1.07	23.14	76.55	18.96
	2	1.08	22.96	77.11	19.11
	3	1.08	23.12	76.69	19.15
	4	1.09	23.10	75.72	19.03
	5	1.07	22.61	78.58	19.10
	6	1.11	22.94	76.47	19.36
	7	1.09	23.13	76.09	19.11
	14	1.09	23.14	75.73	19.07
	21	1.09	23.17	75.22	18.97
	30	1.09	22.92	76.01	19.00
	45	1.09	22.50	77.32	18.88
	60	1.08	22.50	77.44	18.90
	75	1.09	23.11	75.05	18.93
	90	1.08	23.18	74.94	18.84
	105	1.09	22.94	75.75	18.78
	120	1.09	23.08	74.72	18.78
	135	1.09	22.89	75.02	18.74
	150	1.09	22.79	75.06	18.66
	185	1.08	22.34	75.48	18.08
	215	1.07	21.91	76.74	18.06

	245	1.05	22.44	75.82	17.80
	275	1.07	22.46	74.79	18.02
	305	1.07	22.28	74.05	17.70
	335	1.07	22.47	73.32	17.52
	365	1.07	22.38	72.95	17.51
	0	1.11	22.96	77.91	19.90
	1	1.12	23.11	77.19	19.95
	2	1.11	22.98	78.40	20.00
	3	1.11	22.96	78.50	20.07
	4	1.12	23.05	78.44	20.22
	5	1.11	23.18	78.53	20.21
	6	1.12	23.17	78.07	20.29
	7	1.12	23.03	79.14	20.43
	14	1.14	23.11	79.02	20.76
	21	1.13	23.13	77.84	20.41
	30	1.12	22.89	78.19	20.00
	45	1.11	23.00	78.26	20.02
PbS	60	1.11	23.03	78.26	20.06
	75	1.12	22.91	77.67	19.91
	90	1.11	23.03	78.79	20.04
	105	1.12	22.82	78.32	20.03
	120	1.11	22.90	78.68	20.02
	135	1.12	22.91	77.90	19.92
	150	1.11	22.87	78.33	19.89
	185	1.12	22.87	77.28	19.73
	215	1.11	22.74	76.91	19.32
	245	1.11	22.31	77.46	19.22
	275	1.11	22.46	77.18	19.27
	305	1.09	22.80	76.90	19.15
	335	1.11	22.78	77.14	19.35
	365	1.11	22.63	77.86	19.39

Table S5. The key photovoltaic parameters of the PSCs with and without PbS QDs for different perovskite layer, Related to Figure 5

Perovskite	Eg (eV)	passivation	V_{OC} (mV)	J_{SC} (mA cm^{-2})	*FF* (%)	*PCE* (%)
$FAPbI_3$	1.48	Pristine	979	22.78	71.59	15.97
		PbS	993	22.64	74.93	16.84
$Cs_{0.15}FA_{0.85}Pb(I_{0..6}Br_{0.4})_3$	1.76	Pristine	1157	18.52	75.95	16.28
		PbS	1173	18.85	78.46	17.35
$Cs_{0.15}FA_{0.85}Pb(I_{0.85}Br_{0.1}Cl_{0.05})_3$	1.63	Pristine	1107	23.08	74.42	19.02
		PbS	1129	23.13	76.75	20.06
$Cs_{0.05}(FA_{0.85}MA_{0.15})_{0.95}Pb(I_{0.85}Br_{0.15})_3$	1.64	Pristine	1110	23.07	72.85	18.66
		PbS	1133	23.08	77.48	20.27

Transparent Methods

Materials: All the chemicals were used as received. Oleic acid (OA, 90%) and Bis(trimethylsilyl) sulfide (TMS) were purchased from Sigma-Aldrich; 1-Octadecene (ODE, 90%) were obtained from Alfa Aesar; Lead iodide (≥98%, TCI, Tokyo Chemical Industry); Cesium iodide (≥99.9%, Sigma-Aldrich); Lead bromide (≥98%, Sigma-Aldrich); $HC(NH_2)I$ (FAI), $HC(NH)_2Br$ (FABr), and spiro-OMeTAD were purchased from Xi'an p-oled. All the solvents were purchased from Aladdin and used without purification.

Synthesis of PbS quantum dots: The PbS QDs was synthesized according to a widely adopted hot-injection colloidal solution approach(Barkhouse et al., 2011). Briefly, 2 mmol (446 mg) PbO, 1.7 mL OA, 20 mL ODE, dried at 100 °C for 2 h, heated to 125 °C, 2 mL ODE containing 1 mmol (212 μL) TMS was injected into this solution, and then naturally cooled to room temperature. The resulting QDs were washed by hexane/isopropanol (1:3), and then dispersed into anisole for later use.

Device Fabrication and Characterization: Devices were prepared on cleaned and patterned FTO substrates. The dense TiO_2 was prepared via hydrothermal treatment of 0.2 M $TiCl_4$ at 70 °C for 1 h. And then the film was washed with ethanol and annealed at 150 °C for 1 h. The perovskite layer was deposited by spin-coating method in a nitrogen filled glovebox. The precursor solution is comprised of 52 mg of CsI, 174 mg of FAI, 560 mg of PbI_2, 50 mg of $PbBr_2$, 15 mg of FABr in 1 mL of dimethyl formamide (DMF) and dimethylsulfoxide (DMSO) (4:1, v/v). The solution was spin-coated onto the dense TiO_2 substrates by a consecutive two-step spin-coating process at 1000 and 5000 rpm for 10 and 40 s, respectively. During the second spin-coating step, 100 μL anisole with different concentration of PbS (0, 0.03, 0.05, 0.1, 0.3, 0.5 mg mL^{-1}) was dropped onto the substrate after 20 s. And then the substrate was annealed at 100 °C for 20 min. After cooling to room temperature, hole transport material solution was spin coated onto perovskite films at 5000 rpm for 30 s in glove box, where the solution of spiro-OMeTAD/chlorobenzene (72.3 mg mL^{-1}) was prepared by adding 28.8 μL 4-tert-butylpyridine and 17.5 μL Li-TFSI/acetonitrile (520 mg mL^{-1}). Finally, 100 nm thick gold electrodes were deposited by thermal evaporation.

The top-view and the cross-sectional SEM images were obtained by using a Titachi S5200 field-emission scanning electron microscope (Hitachi High Technologies Corporation). The quantum dots morphology is examined by transmission electron microscopy (Carl Zeiss SMT Pte, Ltd Libra 200FE) at 200 kV. The UV visible spectra were measured using an Evolution™ 201 spectrophotometer (Thermo fisher scientific Corporation). The XRD was measured on Maxima 7000 diffractometer (Shimadzu, Japan) with a Cu Ka radiation (40 kV, 100 mA). The steady PL spectra and time-resolved PL decay measurements were performed using an HORIBA DeltaFlex system (HORIBA) with an excitation wavelength at 510 nm. Repetition rate were 100 MHz and 2 MHz, respectively. The atomic force microscopy (AFM) date was obtained on a Dimension Icon (broker Corporation). Calibrating of Roughness value, root-mean-square (RMS), and Graphics processing were taken on NanoScope Analysis. TOF-SIMS data were investigated using a time-of-flight SIMS (IONTOF TOF-SIMS 5, EAG Laboratories). The current-voltage characteristics were measured by Keithley 2400 source and the solar simulator with standard AM 1.5G (100mW/cm^2, SSF5-3A: Enlitech) under ambient conditions. The *J-V* curves were measured by forward (-0.1 V to 1.2 V forward bias) or reverse (1.2 V to -0.1 V) scans. *J-V* curves for all devices were obtained by masking the cells with a metal mask 0.09 cm^2 in area. Monochromatic incident photon-to-current conversion efficiency (IPCE) spectra were recorded as functions of wavelength with a monochromatic incident light of 1x1016 photons cm^{-2} in alternating current mode with a bias voltage of 0 V (QE-R3011). The light intensity of the solar simulator was calibrated by a standard silicon solar cell provided by PV Measurements. Electrochemical impedance spectroscopy (EIS) was obtained by using a multi-channel potentiostat (VMP3, Biologic) under dark conditions in the frequency range from 1 MHz to 100 mHz with an AC amplitude of 30 mV. The trap density measurement by thermal admittance spectroscopy (TAS). The experiments were performed using a multi-channel potentiostat (VMP3, Biologic) with frequencies between 10 to 10^6 Hz. The energy profile of trap density of states (tDOS) can be derived from the angular frequency dependent capacitance with the equation:

$$N_t(E_\omega) = -(V_{bi} / qWk_BT)(dC_\omega / d\ln\omega)$$

where C is the capacitance, ω is the angular frequency, q is the elementary charge, k_B is the Boltzmann constant and T is the temperature. V_{bi} and W are the built-in potential and depletion width, respectively, which were extracted from the Mott-Schottky analysis. The applied angular frequency ω defines an energetic demarcation,

$$E_{\omega} = k_B T \ln\left(\frac{\omega_0}{\omega}\right)$$

Where ω_0 is the attempt-to-escape frequency.

Supplemental References

Etgar, L., Gao, P., Qin, P., Graetzel, M., and Nazeeruddin, M.K. (2014). A hybrid lead iodide perovskite and lead sulfide QD heterojunction solar cell to obtain a panchromatic response. J. Mater. Chem. A. *2*, 11586-11590.

Yang, Z., Janmohamed, A., Lan, X., García de Arquer, F.P., Voznyy, O., Yassitepe, E., Kim, G.-H., Ning, Z., Gong, X., Comin, R., et al. (2015). Colloidal Quantum Dot Photovoltaics Enhanced by Perovskite Shelling. Nano Lett. *15*, 7539-7543.

Zhang, X., Zhang, J., Phuyal, D., Du, J., Tian, L., Öberg, V.A., Johansson, M.B., Cappel, U.B., Karis, O., Liu, J., et al. (2018). Inorganic $CsPbI_3$ Perovskite Coating on PbS Quantum Dot for Highly Efficient and Stable Infrared Light Converting Solar Cells. Adv. Energy Mater. *8*, 1702049.

Zhang, Z., Chen, Z., Yuan, L., Chen, W., Yang, J., Wang, B., Wen, X., Zhang, J., Hu, L., Stride, J.A., et al. (2017). A New Passivation Route Leading to Over 8% Efficient PbSe Quantum-Dot Solar Cells via Direct Ion Exchange with Perovskite Nanocrystals. Adv. Mater. *29*, 1703214.

Qi, J., Xiong, H., Wang, G., Xie, H., Jia, W., Zhang, Q., Li, Y., and Wang, H. (2018). High-performance solar cells with induced crystallization of perovskite by an evenly distributed CdSe quantum dots seed-mediated underlayer. J Power Sources. *376*, 46-54.

Zeng, X., Zhou, T., Leng, C., Zang, Z., Wang, M., Hu, W., Tang, X., Lu, S., Fang, L., and Zhou, M. (2017). Performance improvement of perovskite solar cells by employing a CdSe quantum dot/PCBM composite as an electron transport layer. J. Mater. Chem. A. *5*, 17499-17505.

Ali, S.M., Ramay, S.M., Aziz, M.H., ur-Rehman, N., AlGarawi, M.S., AlGhamd, S.S., Mahmood, A., Alkhuraiji, T.S., and Atiq, S. (2018). Efficiency enhancement of perovskite solar cells by incorporation of CdS quantum dot through fast electron injection. Org Electron. *62*, 21-25.

Xiao, J.-W., Ma, S., Yu, S., Zhou, C., Liu, P., Chen, Y., Zhou, H., Li, Y., and Chen, Q. (2018). Ligand engineering on CdTe quantum dots in perovskite solar cells for suppressed hysteresis. Nano Energy. *46*, 45-53.

Han, J., Yin, X., Nan, H., Zhou, Y., Yao, Z., Li, J., Oron, D., and Lin, H. (2017). Enhancing the Performance of Perovskite Solar Cells by Hybridizing SnS Quantum Dots with $CH_3NH_3PbI_3$. Small. *13*, 1700953.

Ma, Y., Vashishtha, P., Shivarudraiah, S.B., Chen, K., Liu, Y., Hodgkiss, J.M., and Halpert, J.E. (2017). A Hybrid Perovskite Solar Cell Modified With Copper Indium Sulfide Nanocrystals to Enhance Hole Transport and Moisture Stability. Solar RRL. *1*, 1700078.

Khanzada, L.S., Levchuk, I., Hou, Y., Azimi, H., Osvet, A., Ahmad, R., Brandl, M., Herre, P., Distaso, M., Hock, R., et al. (2016). Effective Ligand Engineering of the Cu_2ZnSnS_4 Nanocrystal Surface for Increasing Hole Transport Efficiency in Perovskite Solar Cells. Adv. Funct. Mater. *26*, 8300-8306.

Xu, L.-Y., Cao, Z.-Q., Zhao, P., and Zhou, C. (2017). A new monocular vision measurement method to estimate 3D positions of objects on floor. International Journal of Automation and Computing. *14*, 159-168.

Tavakoli, M.M., Tavakoli, R., Nourbakhsh, Z., Waleed, A., Virk, U.S., and Fan, Z. (2016). High Efficiency and Stable Perovskite Solar Cell Using ZnO/rGO QDs as an Electron Transfer Layer. Adv. Mater. Interfaces. *3*, 1500790.

Wu, T., Zhen, C., Wu, J., Jia, C., Haider, M., Wang, L., Liu, G., and Cheng, H.-M. (2019). Chlorine capped SnO_2 quantum-dots modified TiO_2 electron selective layer to enhance the performance of planar perovskite solar cells. Sci Bull. *64*, 547-552.

Tu, Y., Wu, J., Zheng, M., Huo, J., Zhou, P., Lan, Z., Lin, J., and Huang, M. (2015). TiO_2 quantum dots as superb compact block layers for high-performance $CH_3NH_3PbI_3$ perovskite solar cells with an efficiency of 16.97%. Nanoscale. *7*, 20539-20546.

Wang, Q., Zhang, X., Jin, Z., Zhang, J., Gao, Z., Li, Y., and Liu, S.F. (2017). Energy-Down-Shift $CsPbCl_3$:Mn Quantum Dots for Boosting the Efficiency and Stability of Perovskite Solar Cells. Acs Energy Lett. *2*, 1479-1486.

Akin, S., Altintas, Y., Mutlugun, E., and Sonmezoglu, S. (2019). Cesium lead based inorganic perovskite quantum-dots as interfacial layer for highly stable perovskite solar cells with exceeding 21% efficiency. Nano Energy. *60*, 557-566.

Zheng, X., Troughton, J., Gasparini, N., Lin, Y., Wei, M., Hou, Y., Liu, J., Song, K., Chen, Z., Yang, C., et al. (2019). Quantum Dots Supply Bulk- and Surface-Passivation Agents for Efficient and Stable Perovskite Solar Cells. Joule. *3*, 1963-1976.

Liu, C., Hu, M., Zhou, X., Wu, J., Zhang, L., Kong, W., Li, X., Zhao, X., Dai, S., Xu, B., et al. (2018). Efficiency and stability enhancement of perovskite solar cells by introducing $CsPbI_3$ quantum dots as an interface engineering layer. Npg Asia Mater. *10*, 552-561.
Barkhouse, D.A.R., Debnath, R., Kramer, I.J., Zhitomirsky, D., Pattantyus-Abraham, A.G., Levina, L., Etgar, L., Grätzel, M., and Sargent, E.H. (2011). Depleted Bulk Heterojunction Colloidal Quantum Dot Photovoltaics. Adv. Mater. *23*, 3134-3138